Title: Quantitative metabolic reference for healthy human cerebrum derived from group averaged 9.4T ^{1}H MRSI data

Authors: Andrew Martin Wright[1,2], Theresia Ziegs[1,2], Anke Henning[1,3]

1. High-Field Magnetic Resonance, Max Planck Institute for Biological Cybernetics, Tübingen, Germany
2. IMPRS for Cognitive & Systems Neuroscience, Tübingen, Germany
3. Advanced Imaging Research Center, UT Southwestern Medical Center, Dallas, Texas, USA

Highlights:

- Quantitative whole cerebrum metabolite maps in the human brain acquired at 9.4 T.
- Group averaged regional metabolite concentrations.
- Group summed regional metabolite spectra.

Abstract: Drawing inspiration from previous works using ^{1}H FID MRSI, this study quantifies metabolite concentrations at 9.4 T in the human cerebrum of a volunteer cohort and performs a respective group analysis to derive region specific metabolite concentrations. Voxel-specific corrections were performed for both water and individual metabolites, as well as used tissue specific T_1-relaxation times. Anatomical and magnetic resonance spectroscopic imaging data were collected using MP2RAGE and FID MRSI sequences, and subsequent data underwent a series of preprocessing techniques. Results showed consistent metabolite maps for key metabolites (NAA, tCr, Glu, tCho and mI), while instability in data quality was noted for lower slices. This study not only showcases the potential of metabolite quantification and mapping at 9.4 T but also underscores the necessity for meticulous data processing to ensure accurate metabolite representations. Comparisons with earlier works and single voxel results validate the methodologies adopted.

1. Introduction:

Molecular imaging of the human brain using proton magnetic resonance spectroscopic imaging (^{1}H MRSI) offers a unique opportunity to explore metabolite distributions across the human brain as well as estimate concentrations of these metabolites in multiple brain regions. The development of ^{1}H MRSI capabilities is a continual process of technical development marked by reducing acquisition times(Bogner et al., 2020) while also improving image resolutions (Nassirpour et al., 2016), enhancing spectral resolutions, and providing reproducible and accurate results (Gasparovic et al., 2006; Hangel et al., 2021; Maudsley et al., 2009; Wright, Murali Manohar, et al., 2021; Ziegs et al., 2023). Improvements in ^{1}H MRSI have emphasized its value as a diagnostic tool for neurodegenerative diseases such as multiple sclerosis (Heckova et al., 2022), glioma (Gruber et al., 2017; Hangel et al., 2020; Laino et al., 2020), epilepsy (Pan et al., 2013), and more (Maudsley et al., 2020; Öz et al., 2014).

In order to facilitate a wider-spread use of ^{1}H MRSI in clinical decision making, establishing guidelines (i.e. a respective metabolic reference atlas) for typical metabolite concentration ranges and their respective spatial distribution in the healthy brain versus different brain disorders is required. Numerous single voxel ^{1}H MRS investigations in the healthy human brain and different brain disorders have been performed but

are typically limited to few pre-selected brain regions and impacted by mixing grey and white matter as well as functionally distinct cortices into the same spectroscopy voxel. Previous pioneering work by (Maudsley et al., 2009) derived whole brain metabolite concentration distributions for N-acetyl-aspartate (NAA), choline containing compounds (Cho) and Creatine (Cr) from a group analysis of high-resolution whole brain ^{1}H MRSI data acquired at 3 T in 80 healthy volunteers.

Previous studies using ^{1}H MRSI at ultra-high field (UHF, field strength $\geq$ 7 T) strength have demonstrated the potential to map a larger number of brain metabolites at high spatial resolution exploiting the advantages of free induction decay (FID) ^{1}H MRSI sequence that minimizes SAR and reduces acquisition time for fully sampled data (Bogner et al., 2020). ^{1}H FID MRSI at UHF has unambiguous advantages including increased spectral resolution and increased SNR, or these advantages can be traded for faster acquisition times (Bogner et al., 2012; Henning, 2017; Henning et al., 2009; Nassirpour, Chang, & Henning, 2018; Nassirpour, Chang, Avdievitch, et al., 2018). The ^{1}H FID MRSI approach has been successfully translated to a 9.4 T human whole-body MRI scanner and enabled reliable data quality (Nassirpour et al., 2016). Furthermore, 9.4 T studies have investigated full brain reproducibility (Ziegs et al., 2023) and single slice quantitative analysis (Wright et al., 2022) of ^{1}H MRSI of the human brain at 9.4 T.

This work melds previous 9.4 T ^{1}H FID MRSI efforts to provide group averaged metabolite distribution maps across the human cerebrum as metabolic reference. A respective dedicated data analysis pipeline has been developed and serves as a trail blazer toward the establishment of a metabolic atlas based on larger data sets in future. The same multi-slice 2D acquisition technique was used in this work as an extension of prior 9.4 T ^{1}H FID MRSI studies (Nassirpour et al., 2016; Wright et al., 2022; Ziegs et al., 2023); a simulated relaxation corrected macromolecule baseline was included in metabolite fitting (Wright, Murali-Manohar, et al., 2021); and full T_1-corrections were utilized to correct for T_1-weighting that accompanied the short TR of this work (Wright et al., 2022). We combined MRSI data sets and respective individual metabolite maps from different volunteers into group averaged ones for the first time at 9.4 T to showcase how MRSI could be utilized in clinical studies where comparisons between healthy controls and diseased cohorts are researched. We hence demonstrate the potential of 9.4 T MRSI in elucidating the quantitated neurochemical profiles in the human cerebrum and provide reference metabolite concentrations for different brain regions.

2. Methods:

10 healthy volunteers were measured on a 9.4 T whole body scanner (Siemens Magnetom, Erlangen, Germany). A local ethics committee approved acquisition of data in human volunteers, and all volunteers provided written consent prior to scanning. Volunteers were asked to participate for as long as comfortable with a maximum allowable scan duration of two hours inside of the scanner. 8 data sets were useable for analysis; both excluded data sets were due to subject motion which yielded incomplete and non-analyzable data sets. All volunteers were measured using the same dual-row (18Tx/32Rx) phased array head coil (Avdievich et al., 2018).

2.1 Acquisition:

High-resolution (0.6 x 0.6 x 0.6 mm^3) anatomical MP2RAGE images were acquired at the beginning of each scan session (TI1/TI2 = 900/3500 ms, FA=4/6°,TR = 6 ms, TE = 2.3 ms, TA = 11 min). Full details of the sequence are described by (Hagberg et al., 2017) with a matched fast AFI map (Pohmann &

Scheffler, 2013; Yarnykh, 2007) (resolution: 3.3 x 3.3 x 3.3 mm^3, FA = 50°, TE/TR_1/TR_2 = 4/20/100 ms, TA = 1 min 20 sec) to correct for B_1^+ inhomogeneity related distortions.

Metabolite and water reference data were acquired with a ^{1}H FID MRSI sequence using an acquisition delay (TE*) of 1.3 ms, a TR of 300 ms, a flip angle of 47°, and elliptical k-space shuttering. Metabolite spectra utilized an optimized water suppression scheme with three unmodulated Hanning-filtered Gaussian pulses (BW = 180 Hz, duration = 5 ms) with flip angles of 90°, 79.5°, and 159°; the inter-pulse delay between all pulses was 20 ms. MRSI and water reference data were acquired with a 6 x 6 x 6 mm^3 resolution. For a slice dimension of 210 x 210 x 6 mm^3 the acquisition time (TA) was approximately 4.5 min; resulting in approximately 9 min per slice. 2nd-order vendor-implemented image based B_0 shimming was used in blocks to reduce the overall scan time. In most cases, four blocks were sufficient to B_0 shim the full brain: three blocks with 3 to 5 slices each dividing the cerebrum and a fourth block with 4 to 6 slices for cerebellum data.

Full brain coverage including the cerebellum was planned during data acquisition. However, due to insufficient data quality in lower slices, this study is limited to the metabolic analysis of the cerebrum only. Poor data quality in lower brain slices has also been reported by an earlier study (Ziegs et al., 2023) while using the same RF coil setup and B_0 shimming method at 9.4T and can be attributed to insufficient SNR for metabolite data due to a limitation of the longitudinal RF coil coverage along with broad linewidth due to insufficient B_0 shimming. The total slices acquired for each volunteer ranged from 11 to 17 slices depending on the head size and shape.

2.2 Preprocessing:

^{1}H MRSI data were reconstructed using a spatial Hanning filter before the 2D FFT, then eddy current corrected (Klose, 1990), and coil combined using the singular value decomposition (SVD) method (Bydder et al., 2008). Data were then further processed to remove residual water using the Hankel-Lanczos (HLSVD) (Cabanes et al., 2001) method with 10 decaying sinusoids in the range of 4.4-5 ppm. 1st-order phase correction was performed using a linear back prediction of the missing FID points (Kay, 1988). L2-regularization for retrospective skull lipid removal (Bilgic et al., 2014) was performed uniformly on all data sets using findings from (Ziegs et al., 2023). Spectroscopic imaging data from individual volunteers was then fitted as outlined in section 2.3.

2.3 Group averaged metabolite maps:

Data were fitted in LCModel (Provencher, 2001) from 0.8 to 4.2 ppm using a simulated basis set with 12 metabolites : N-acetyl-aspartate (NAA), total creatine (tCr), aspartate (Asp), γ-aminobutyric acid (GABA), taurine (Tau), glutamine (Gln), glutamate (Glu), glutathione (GSH), myo-inositol (mI), scyllo-inositol (Scyllo), N-acetyl-aspartyl-glutamate (NAAG), and phosphocholine + glycerophosphocholine (tCho) plus a simulated MM spectrum (MM_{AXIOM}, (Wright, Murali-Manohar, et al., 2021; Wright, Murali Manohar, et al., 2021)) to account for MM contributions. After spectral fitting, data were quantified using a voxel-specific correction method considering relaxation correction of metabolites and water as described in (Wright et al., 2022) yielding metabolite maps in mmol kg^{-1} (Figure 1) and mM (presented in Supporting Information).

Following quantification, quantitative metabolite maps were interpolated to match the MP2RAGE spatial resolution and written to the nifti file format (.nii) as preparatory step for linear co-registration calculations to be performed in FSL (Jenkinson et al., 2012). These quantitative metabolite maps were

then co-registered to the MNI152 Human Brain atlas (2mm resolution) using FSL FLIRT by transforming the MP2RAGE to the standardized space and having all metabolite maps be secondary transformations. The FLIRTed metabolite maps were then used for calculation of average and median metabolite and CRLB maps.

Brain regions were partitioned using three atlases (Harvard-Oxford maximum probability cortical atlas [2 mm], Harvard-Oxford maximum probability subcortical atlas [2 mm], and Johns Hopkins University,

Metabolite Quality Control Metrics												
	NAA	tCr	Glu	mI	tCho	Gln	NAAG	Asp	GABA	GSH	Tau	Scyllo
CRLB Cutoff (% SD)	10	20	50	50	20	50	100	80	80	80	50	100
Minimum Concentration [mmol kg^{-1}]	3	2	2	1	0.1	0.01	0.1	0.01	0.01	0.01	0.1	0.1

Table 1: Maximum CRLB cutoffs and minimum concentrations for metabolite concentration estimates. The CRLB thresholds were defined as the mean plus SD for each individual metabolite as recommended by the MRS consensus group (Lin et al., 2021).

International Consortium for Brain Mapping template [2mm], (Desikan et al., 2010; Frazier et al., 2005; Goldstein et al., 2007; Hua et al., 2008; Makris et al., 2006; "MRI Atlas of Human White Matter," 2006; Wakana et al., 2007)) and used to calculate concentrations for eight regions in the brain. A full summary of regional combinations is reported in Supporting Information Table 1.

2.4 Brain region specific average spectra and metabolite concentrations:

Eight anatomical regions are reported in this study. These regions were defined by taking atlas data and combining sub-regions into the following major brain regions: frontal lobe GM, frontal lobe WM, parietal lobe GM, parietal lobe WM, occipital lobe GM, occipital lobe WM, temporal lobe GM, and corpus callosum. These combinations are explicitly reported in Supporting Information Table 1 and are shown in Supporting Information Figure 1.

Regional summed spectra were created after transforming the regional masks back to the original space for each volunteer. This was done using the FSL suite and using the inverse of the affine matrix from the forward FLIRT calculation. These masks were then resampled back to the original MRSI resolution (6 x 6 x 6 mm^3), and the indices for non-zero voxels were then used to select spectral data. The .coord output files were used to create the summed spectra. Summed spectra were then evaluated across all slices, and slices that contained little signal or strong lipid distortions were excluded from the summed spectra.

Mean regional concentrations were calculated using quantified metabolite maps following the FSL FLIRT operation. To reduce the impact of spurious spectral fitting, data were filtered for maximum allowable CRLB values and minimum physiological concentrations as a quality measure (Table 1). Concentrations were calculated in mmol kg^{-1} and mM quantities. Concentrations between regions were compared for each metabolite. Mann-Whitney U-tests were carried out for all reported regions with a significance threshold of 0.05 assigned. Bonferroni corrections were applied for each region and used to report corrected p-values for comparisons.

3. Results

3.1 Quantitative Metabolite Maps

Metabolite maps with T_1-corrected and quantitated data for 12 metabolites are reported in Figure 1. The calculated maps are the median from eight volunteers and reported in MNI space with units of mmol kg^{-1}. Metabolite map slices (in MNI space) from 45 and below are reported with an additional scale to reduce oversaturation for some metabolite maps. Metabolite maps in mM quantities are reported in Supporting Information Figure 2**.**

Observable tissue contrast is apparent for tCho, Glu, Gln, mI, NAAG, Glu+Gln, and NAA+NAAG maps. The distribution of metabolite concentrations is consistent with previous 9.4 T reports (Nassirpour et al., 2016; Wright et al., 2022; Ziegs et al., 2023) and lower field strengths (Hangel et al., 2021; Maudsley et al., 2009).

Averaged CRLB maps are shown in Figure 2. The color bar is a non-uniformly spaced binning of CRLB ranges. CRLB maps with maximum thresholds applied are reported in Supporting Information Figure 3. As can be seen in Figure 1 and Figure 2, data in MNI space below slice 45 diminish in quality. CRLB maps show that the median CRLB in lower slices is much higher than acceptable for data reporting. This effect is seen clearly in Figure 1 by areas of signal dropout or overexposure. Metabolite maps presented in sagittal, coronal, and transversal are also reported (Figure 6) and showcased in section 4.1.
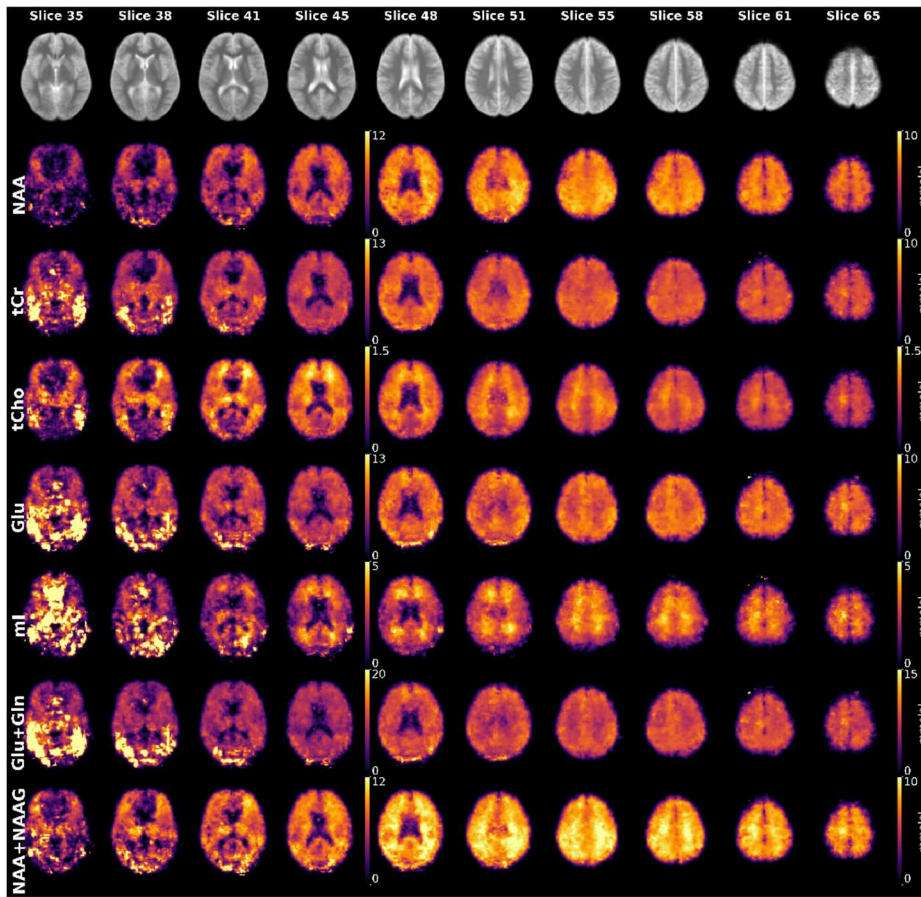
Figure 1: Median metabolite maps of eight volunteers displaying the distribution of all analyzed metabolites. The anatomical data are derived from averaged, T_1-weighted images coregistered to the MNI 152 Human Brain Atlas. The quantitative data, expressed in mmol kg^{-1}, are also coregistered to the same atlas. Slice positions refer to the slice position in MNI space.
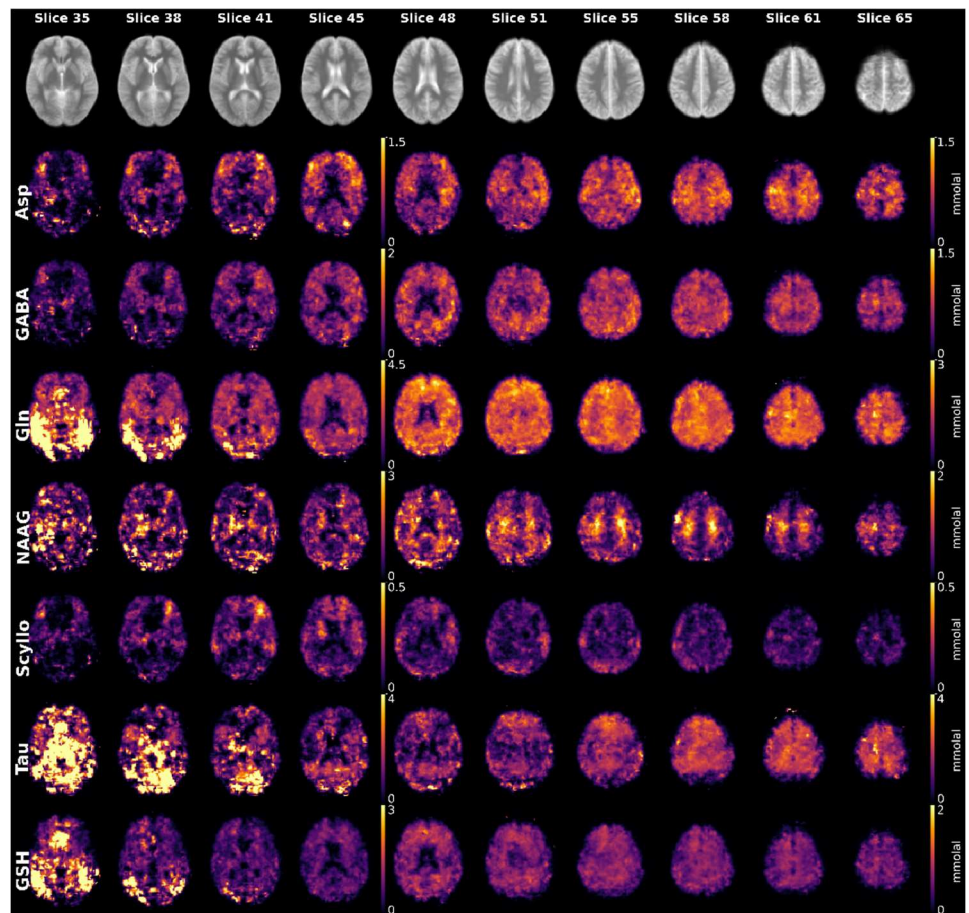
Figure 2: median CRLB (% SD) maps with a non-uniformly binned color bar. These maps do not include the threshold which was applied for metabolite concentration calculations. Maps with this threshold applied are shown in Supporting Information Figure 3. All maps are presented in the MNI 152 space.
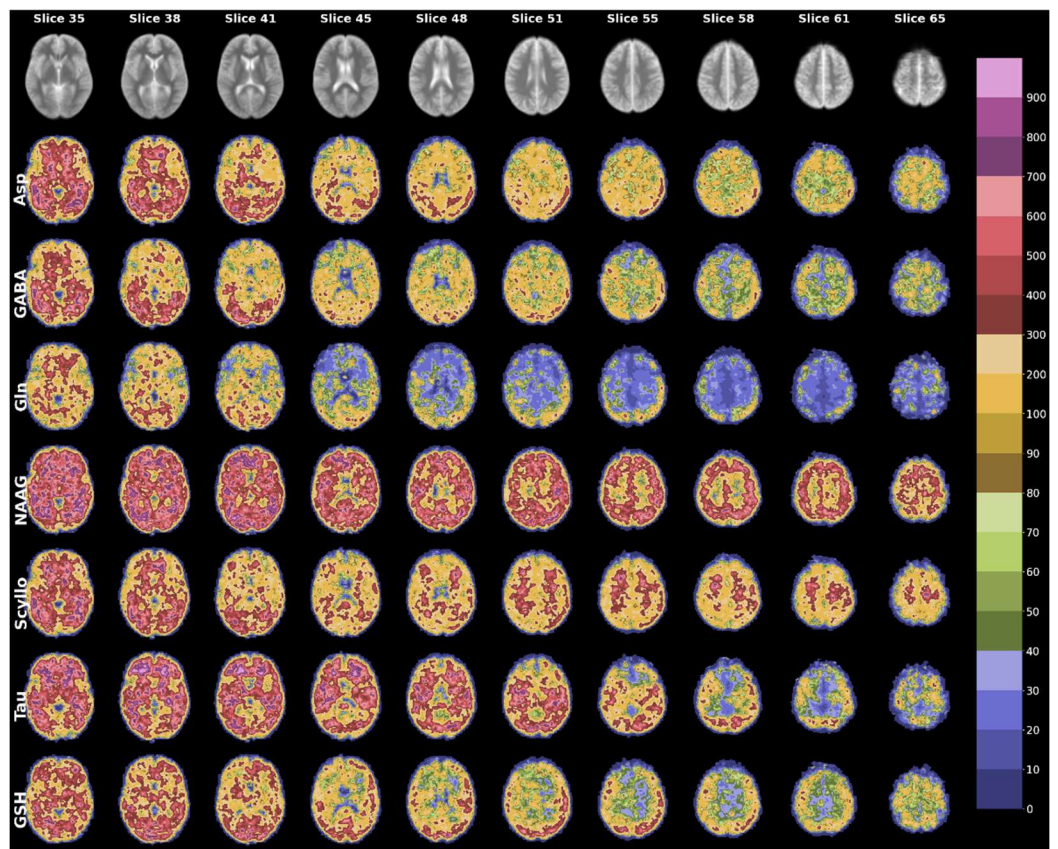
3.2 Regional Metabolite Spectra

The LCModel fits of metabolites were combined to display regional sums for metabolite spectra (Figure 3) where the black line is the spectra data and the red line is the fit data. Estimated regional spectra and concentrations include the following anatomical regions: frontal Lobe GM, frontal Lobe WM, parietal Lobe, parietal Lobe WM, temporal lobe, insular cortex, corpus callosum. All regional masks applied to MNI space images were transformed back to each original space and MRSI resolution and all non-zero signal voxels were summed. The total number of voxels included for each region is listed below the region name in Figure 3.

All regions maintain good spectral resolution. However, regions with more voxels (specifically GM regions) have slightly broader lineshapes.
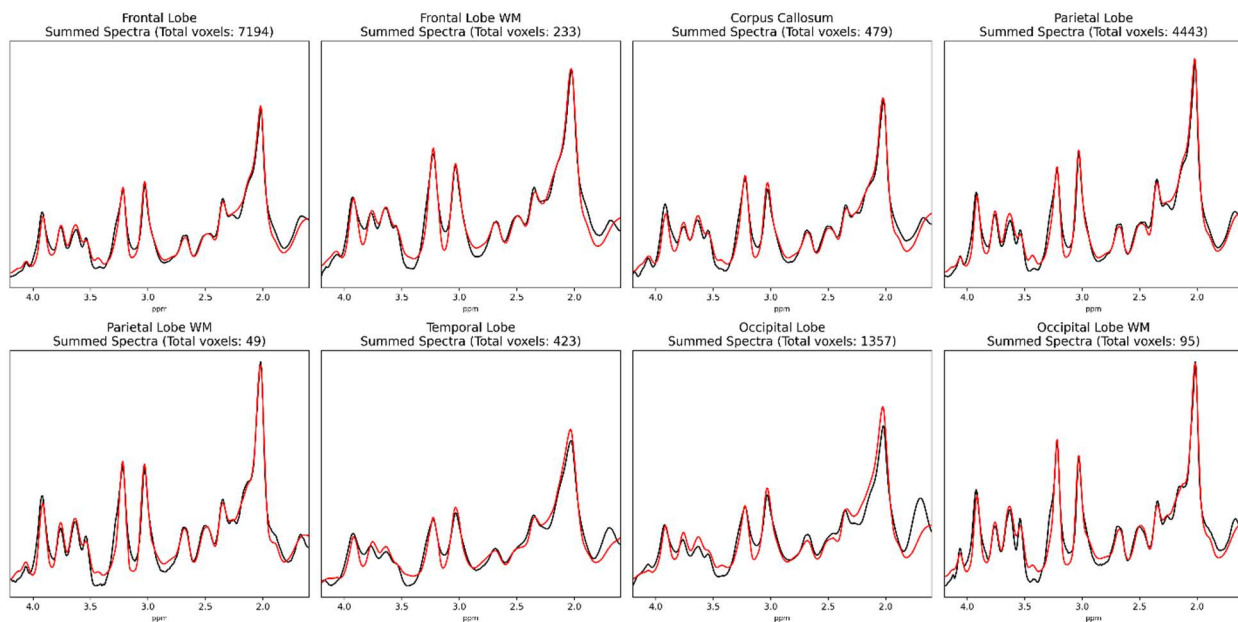
Figure 3: Summed metabolite spectra for each of the eight chosen major brain regions. Data were summed by taking the .coord output files. The black line represents the actual data, and the red line is the sum of fit results for selected voxels.

3.3 Regional Metabolite Concentrations

Metabolite concentrations [mmol kg^{-1}] for eight brain regions are reported in Table 2 and statistical differences marked by numerical superscripts to note significance between regions (Regional Key for statistical comparisons, Table 3) and visually represented in Figure 4. 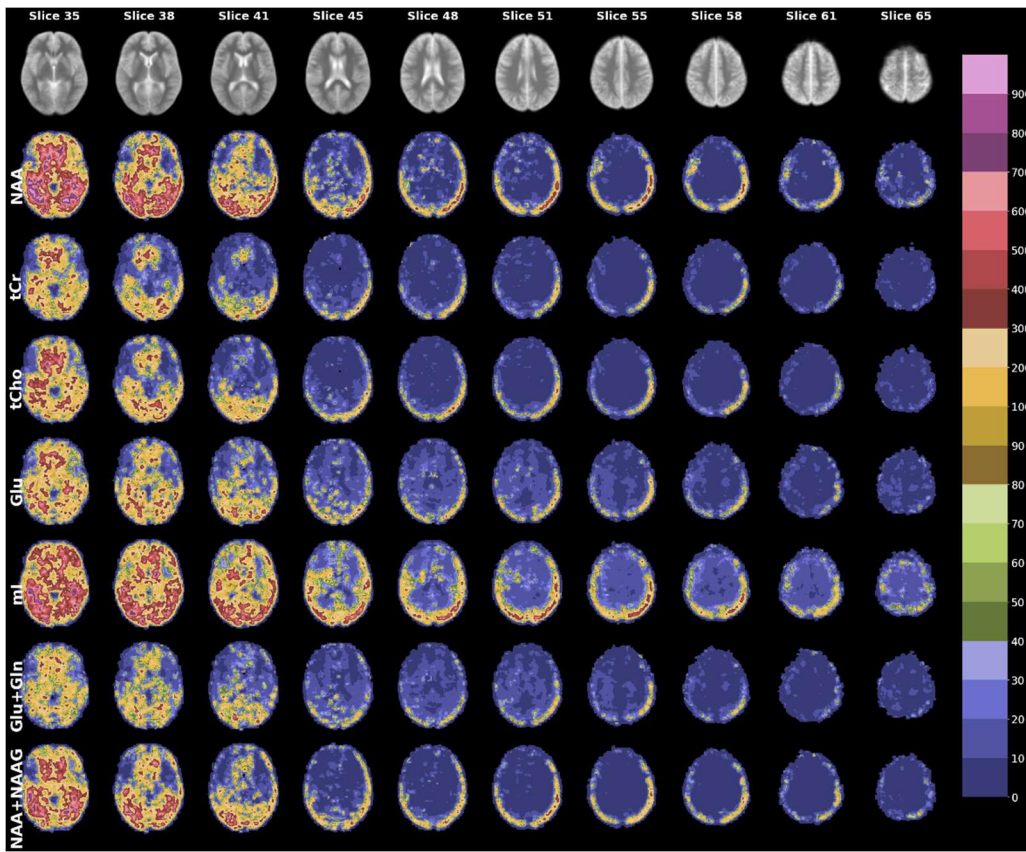Metabolite concentrations were calculated in the MNI152 space by masking quantitative metabolite maps with a regional mask. Concentrations are in general agreement with previous work at 9.4 T (Nassirpour et al., 2016; Wright et al., 2022; Ziegs et al., 2023). However, there are some slight differences that are discussed further in section 4.2 with violin plots (Figure 5) to show distributions of metabolite concentrations taken from the masked quantified metabolite maps.

Inter-subject coefficients of variation (CVs) were calculated using mmol kg^{-1} metabolite maps and are reported in Table 4, and corrected p-values from Mann-Whitney U-tests are reported and shown in

Figure 4. All p-values less than 0.05 are highlighted in yellow. Regional metabolite concentration distributions are shown in Figure 6 via violin plots and discussed in section 4.2. Please refer to Supporting Information Table 4 for an additional representation of regional metabolite concentration differences.

Metabolite Concentrations [mmol kg⁻¹]								
	Frontal Lobe GM	Temporal Lobe GM	Parietal Lobe GM	Occipital Lobe GM	Frontal Lobe WM	Occipital Lobe WM	Parietal Lobe WM	Corpus Callosum
NAA[2,3,7,8,16,17,19,21,24,28]	9.39 ± 0.73	9.99 ± 0.66	10.23 ± 0.69	10.40 ± 1.20	11.16 ± 0.34	11.27 ± 0.69	12.4 ± 0.62	8.64 ± 1.47
tCr[2,3,8,12,17,23]	7.57 ± 0.32	10.76 ± 6.33	8.48 ± 0.37	8.02 ± 0.74	9.54 ± 0.66	8.91 ± 0.68	9.50 ± 0.79	7.15 ± 1.08
Glu[5,15,22,26]	8.41 ± 0.39	14.15 ± 12.98	9.07 ± 0.41	8.94 ± 1.48	9.50 ± 0.76	8.05 ± 0.40	9.34 ± 1.51	7.24 ± 1.27
mI[8,10,19]	4.06 ± 0.49	8.65 ± 8.89	4.14 ± 0.41	3.62 ± 0.46	5.24 ± 0.96	5.63 ± 0.99	5.03 ± 0.77	4.36 ± 0.71
tCho[3,6,8,10,13,15,17,19,21,24,26]	1.08 ± 0.08	1.22 ± 0.12	1.14 ± 0.08	1.00 ± 0.14	1.66 ± 0.11	1.57 ± 0.16	1.60 ± 0.12	1.18 ± 0.22
Gln	2.37 ± 0.26	8.01 ± 13.19	2.63 ± 0.33	2.74 ± 1.08	3.22 ± 0.57	3.06 ± 0.72	3.22 ± 0.97	2.29 ± 0.59
NAAG	1.78 ± 0.92	2.80 ± 1.30	1.65 ± 0.54	2.07 ± 0.79	3.09 ± 1.49	2.47 ± 0.60	2.92 ± 1.05	2.26 ± 0.96
Asp[3,6,19,24,28]	1.02 ± 0.18	0.82 ± 0.26	1.12 ± 0.27	0.80 ± 0.40	1.63 ± 0.31	1.33 ± 0.38	1.71 ± 0.35	0.92 ± 0.35
GABA[2,3,6,13,16,17,19,24,28]	0.86 ± 0.08	0.85 ± 0.16	1.00 ± 0.10	0.83 ± 0.21	1.38 ± 0.16	1.11 ± 0.27	1.44 ± 0.27	0.83 ± 0.20
GSH[2,3,13,23]	0.96 ± 0.12	3.51 ± 3.84	1.03 ± 0.16	1.08 ± 0.33	1.63 ± 0.34	1.3 ± 0.20	1.28 ± 0.20	1.00 ± 0.23
Tau	2.64 ± 0.51	22.16 ± 26.51	2.76 ± 0.32	2.78 ± 0.91	5.94 ± 7.16	3.41 ± 1.38	4.25 ± 2.01	7.50 ± 14.68
Scyllo[2,3,13,16,17,21]	0.30 ± 0.04	0.36 ± 0.04	0.31 ± 0.03	0.37 ± 0.10	0.44 ± 0.05	0.29 ± 0.07	0.49 ± 0.09	0.28 ± 0.06

Table 2: Metabolite concentrations [mmol kg⁻¹] for the selected eight major brain regions. Regional masks can be found in Supporting Information Figure 1. Metabolite concentrations reported in mM quantities are reported in Supporting Information Table 2. The superscript on metabolites highlights an adjusted p-value < 0.05 between regions as is defined in the Regional Key for Statistical Comparisons (Table 3).

Regional Key for Statistical Comparisons								
Region	**Key Numbers**							
Corpus Callosum								
Frontal Lobe GM	1							
Frontal Lobe WM	2	3						
Occipital Lobe GM	4	5	6					
Occipital Lobe WM	7	8	9	10				
Parietal Lobe GM	11	12	13	14	15			
Parietal Lobe WM	16	17	18	19	20	21		
Temporal Lobe GM	22	23	24	25	26	27	28	
Region	*Corpus Callosum*	*Frontal Lobe GM*	*Frontal Lobe WM*	*Occipital Lobe GM*	*Occipital Lobe WM*	*Parietal Lobe GM*	*Parietal Lobe WM*	*Temporal Lobe GM*

Table 3: Key to statistical comparisons noted in Table 2 and visually displayed in Figure 4. For example, the number 1 represents a comparison between the Frontal Lobe GM and Corpus Callosum and the number 19 represents a comparison between the Parietal Lobe WM and Occipital Lobe GM.

	Frontal Lobe GM	Temporal Lobe GM	Parietal Lobe GM	Occipital Lobe GM	Frontal Lobe WM	Occipital Lobe WM	Parietal Lobe WM	Corpus Callosum
NAA	5	5	4	6	2	5	4	14
tCr	3	3	3	8	5	6	5	12
Glu	3	3	3	6	5	4	7	11
mI	9	10	8	12	15	15	10	15
tCho	5	6	5	12	6	7	6	16
Gln	8	10	8	14	12	17	14	21
NAAG	15	15	11	18	22	16	18	30
Asp	13	21	20	30	4	22	12	28
GABA	8	12	9	18	7	16	11	19
GSH	10	9	12	13	12	10	12	20
Tau	7	15	5	9	14	31	8	18
Scyllo	5	10	7	16	6	17	12	15

Inter-Subject CV (%)

Table 4: inter-subject coefficients of variation (CV, %)

Bonferroni Corrected P-values

NAA (blue) and NAAG (green)

	CC	FLGM	FLWM	OCGM	OCWM	PLGM	PLWM	TLGM
CC		1.0	1.0	1.0	1.0	1.0	1.0	1.0
FLGM	1.0		1.0	1.0	1.0	1.0	0.5787	1.0
FLWM	0.0174	0.0044		1.0	1.0	0.5787	1.0	1.0
OCGM	0.5787	1.0	1.0		1.0	1.0	1.0	1.0
OCWM	0.0305	0.0044	1.0	1.0		0.4379	1.0	1.0
PLGM	0.5787	1.0	0.5787	1.0	0.5815		0.1305	1.0
PLWM	0.0044	0.0044	0.0522	0.0305	0.0827	0.0044		1.0
TLGM	1.0	1.0	0.0174	1.0	0.1272	1.0	0.0044	

tCr (blue) and tCho (green)

	CC	FLGM	FLWM	OCGM	OCWM	PLGM	PLWM	TLGM
CC		1.0	0.0762	1.0	0.2409	1.0	0.0522	1.0
FLGM	1.0		0.0249	1.0	0.0254	1.0	0.0254	0.4293
FLWM	0.0378	0.0261		0.0258	1.0	0.0256	1.0	0.0309
OCGM	1.0	1.0	0.1498		0.0044	1.0	0.0044	0.2792
OCWM	0.0522	0.0044	1.0	0.7876		0.0261	1.0	0.0305
PLGM	0.2915	0.0044	0.5052	1.0	1.0		0.0261	1.0
PLWM	0.0087	0.0044	1.0	0.0522	1.0	0.4134		0.0645
TLGM	0.2807	0.0378	1.0	1.0	1.0	1.0	1.0	

Glu (blue) and Gln (green)

	CC	FLGM	FLWM	OCGM	OCWM	PLGM	PLWM	TLGM
CC		1.0	0.4379	1.0	1.0	1.0	1.0	0.1958
FLGM	0.4134		0.0827	1.0	0.7876	1.0	0.2915	0.0522
FLWM	0.0827	0.0827		1.0	1.0	0.9956	1.0	1.0
OCGM	0.7876	1.0	1.0		1.0	1.0	1.0	1.0
OCWM	1.0	1.0	0.0174	1.0		1.0	1.0	1.0
PLGM	0.3264	0.1958	1.0	1.0	0.0305		1.0	0.2915
PLWM	0.2915	1.0	1.0	1.0	0.4134	1.0		1.0
TLGM	0.0305	0.0522	1.0	1.0	0.0087	1.0	1.0	

Asp (blue) and GABA (green)

	CC	FLGM	FLWM	OCGM	OCWM	PLGM	PLWM	TLGM
CC		1.0	0.0314	1.0	1.0	1.0	0.0087	1.0
FLGM	1.0		0.0261	1.0	0.3728	0.4357	0.0261	1.0
FLWM	0.0827	0.0261		0.0044	0.3785	0.0314	1.0	0.0044
OCGM	1.0	1.0	0.0305		0.8736	1.0	0.0174	1.0
OCWM	1.0	1.0	1.0	0.6677		1.0	0.6677	1.0
PLGM	1.0	1.0	0.5815	1.0	1.0		0.0645	1.0
PLWM	0.0645	0.1078	1.0	0.0174	1.0	0.1489		0.0087
TLGM	1.0	1.0	0.0044	1.0	0.3785	1.0	0.0087	

mI (blue) and Tau (green)

	CC	FLGM	FLWM	OCGM	OCWM	PLGM	PLWM	TLGM
CC		1.0	1.0	1.0	1.0	1.0	1.0	0.5787
FLGM	1.0		0.4134	1.0	1.0	1.0	0.3543	0.1305
FLWM	1.0	0.4134		1.0	1.0	1.0	1.0	1.0
OCGM	1.0	1.0	0.0827		1.0	1.0	1.0	0.1958
OCWM	0.3264	0.0087	1.0	0.0044		1.0	1.0	0.5789
PLGM	1.0	1.0	0.4134	1.0	0.0453		0.3284	0.3785
PLWM	1.0	1.0	1.0	0.0174	1.0	0.4134		1.0
TLGM	1.0	1.0	1.0	1.0	1.0	1.0	1.0	

GSH (blue) and Scyllo (green)

	CC	FLGM	FLWM	OCGM	OCWM	PLGM	PLWM	TLGM
CC		1.0	0.0254	1.0	1.0	1.0	0.0304	0.6533
FLGM	1.0		0.0254	1.0	1.0	1.0	0.0304	0.752
FLWM	0.0378	0.0044		1.0	0.2025	0.0252	1.0	0.1396
OCGM	1.0	1.0	0.4134		1.0	1.0	0.8562	1.0
OCWM	1.0	0.0827	1.0	1.0		1.0	0.0529	1.0
PLGM	1.0	1.0	0.0261	1.0	0.8736		0.0301	0.9691
PLWM	0.5052	0.0522	0.7647	1.0	1.0	0.4357		0.2701
TLGM	0.0768	0.0174	1.0	0.176	0.3264	0.0768	0.1958	

NAA+NAAG (blue) and Glu+Gln (green)

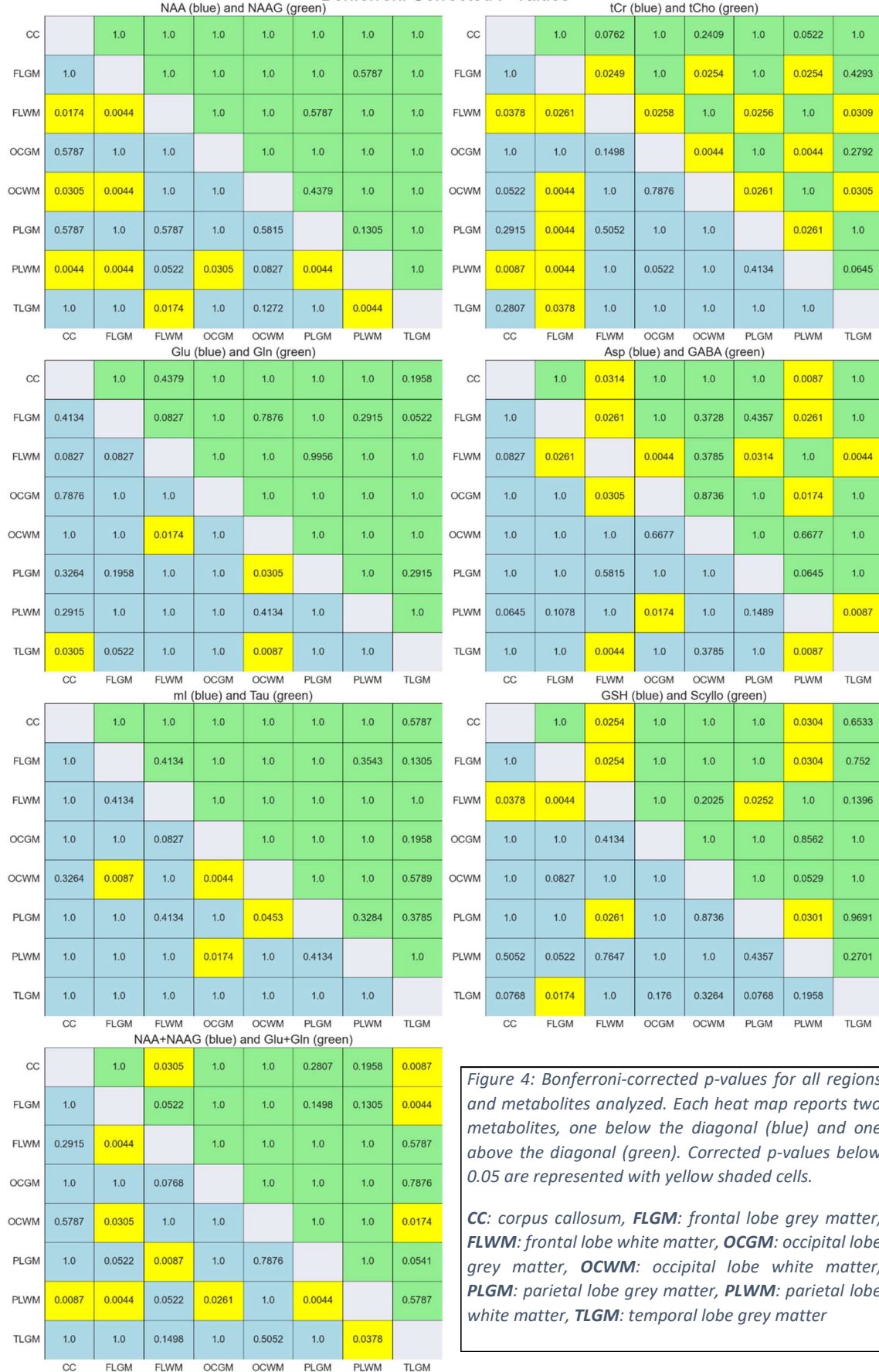|	CC	FLGM	FLWM	OCGM	OCWM	PLGM	PLWM	TLGM
CC		1.0	0.0305	1.0	1.0	0.2807	0.1958	0.0087
FLGM	1.0		0.0522	1.0	1.0	0.1498	0.1305	0.0044
FLWM	0.2915	0.0044		1.0	1.0	1.0	1.0	0.5787
OCGM	1.0	1.0	0.0768		1.0	1.0	1.0	0.7876
OCWM	0.5787	0.0305	1.0	1.0		1.0	1.0	0.0174
PLGM	1.0	0.0522	0.0087	1.0	0.7876		1.0	0.0541
PLWM	0.0087	0.0044	0.0522	0.0261	1.0	0.0044		0.5787
TLGM	1.0	1.0	0.1498	1.0	0.5052	1.0	0.0378	

Figure 4: Bonferroni-corrected p-values for all regions and metabolites analyzed. Each heat map reports two metabolites, one below the diagonal (blue) and one above the diagonal (green). Corrected p-values below 0.05 are represented with yellow shaded cells.

CC: corpus callosum, FLGM: frontal lobe grey matter, FLWM: frontal lobe white matter, OCGM: occipital lobe grey matter, OCWM: occipital lobe white matter, PLGM: parietal lobe grey matter, PLWM: parietal lobe white matter, TLGM: temporal lobe grey matter
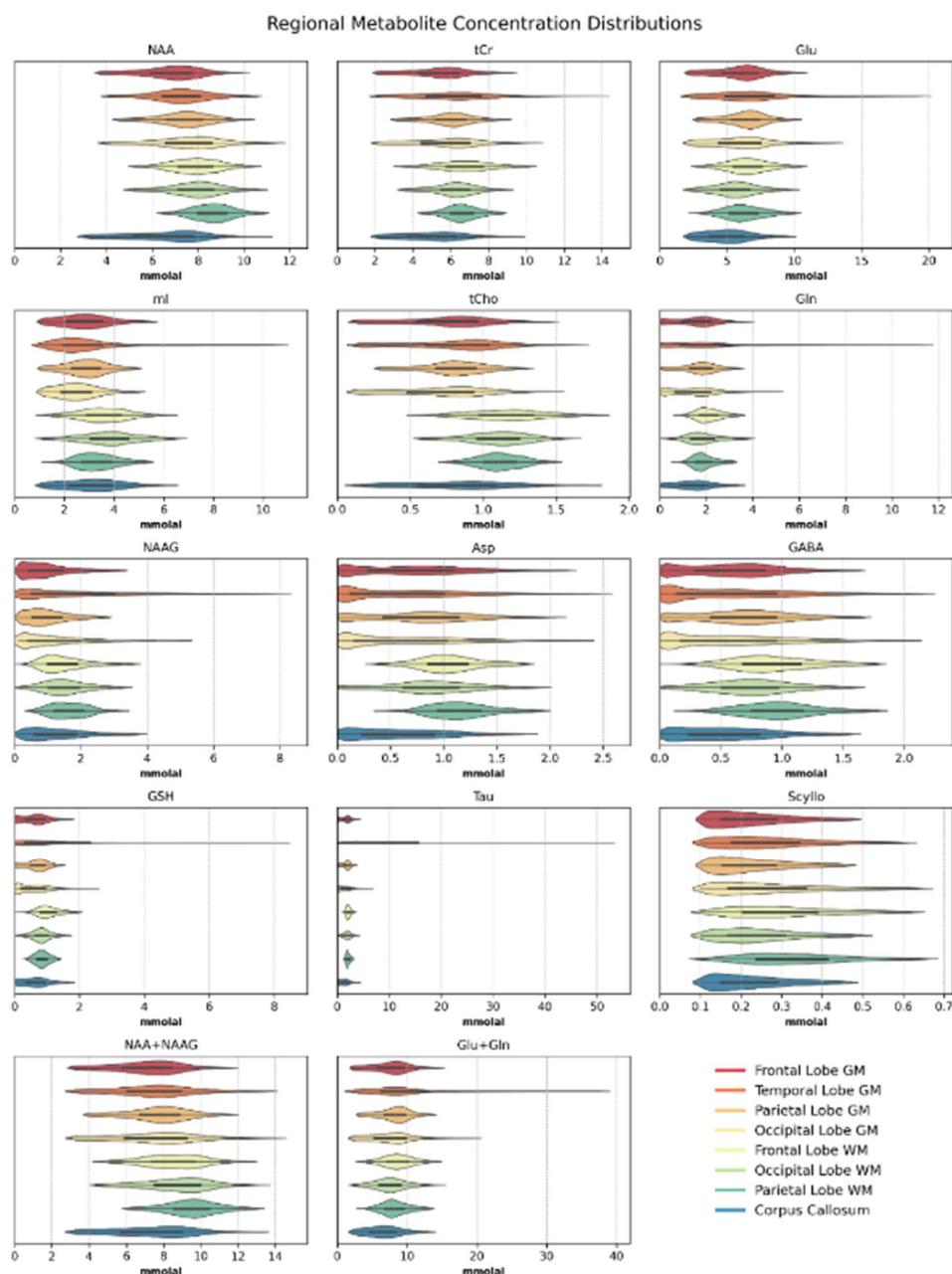
Figure 5: violin plots showing regional metabolite concentrations for eight major brain regions. Data had a CRLB threshold applied (Table 1). These distributions were aggregated in MNI space by applying the regional masks across all volunteers.

4. Discussion

4.1 Metabolite Maps

The metabolite map quality obtained in this study is a step forward aiming at the establishment of a whole brain metabolite concentration reference atlas. In comparison to a previous group analysis study performed at 3T (Maudsley et al., 2009) in a large volunteer cohort demonstrating the spatial distribution of NAA, tCho and tCr a substantially larger number of metabolites could be imaged across the cerebrum herein. Previous whole-brain 7T ^{1}H MRSI studies in single volunteers showed the spatial distribution of only five metabolites: NAA, tCr, tCho, Glx and mI (Hangel et al., 2021) and six metabolites

without quantification: NAA, tCr, tCho, Glu, mI, and NAAG (Klauser et al., 2021). Compared to previous 9.4 T MRSI studies (Nassirpour, Chang, Avdievitch, et al., 2018; Nassirpour et al., 2016; Ziegs et al., 2023), this work shows a comparable quality across the cerebrum and maintained the standard of quantifying concentrations for 12 metabolites in vivo with voxel-specific T_1-weighting corrections. However, the quality of metabolite maps was not sufficient to derive quantitative metabolite maps in lower slices in the brain, which is also evidenced in a recent 9.4 T study (Ziegs et al., 2023) which assessed test-retest reproducibility and brain coverage of ^{1}H MRSI with an identical technical study design. This limitation has also been demonstrated in previous 7T whole-brain ^{1}H MRSI studies (Hangel et al., 2021; Klauser et al., 2021; Motyka et al., 2019). Improving the longitudinal coverage of transmit and receive B_1 fields by improved RF coil design along with tackling the B_0 inhomogeneity in the lower brain by dedicated B_0 shimming software and hardware are likely the most important targets for achieving whole brain ^{1}H FID MRSI coverage at UHF in future.

Metabolite concentration distributions obtained herein agree with previous ^{1}H MRSI studies (Bogner et al., 2012; Hangel et al., 2021; Henning et al., 2009; Maudsley et al., 2009; Nassirpour et al., 2016; Wright et al., 2022; Ziegs et al., 2023). Metabolites with concentrations appearing higher in GM in metabolite maps include: Glu, Gln, and Tau, while metabolites with increased WM concentrations include: NAA, tCho, mI, and NAAG. In the previous 9.4 T quantitative ^{1}H FID MRSI work (Wright et al., 2022), the NAA distribution was not as apparent in the transversal plane; however, in the sagittal and coronal planes
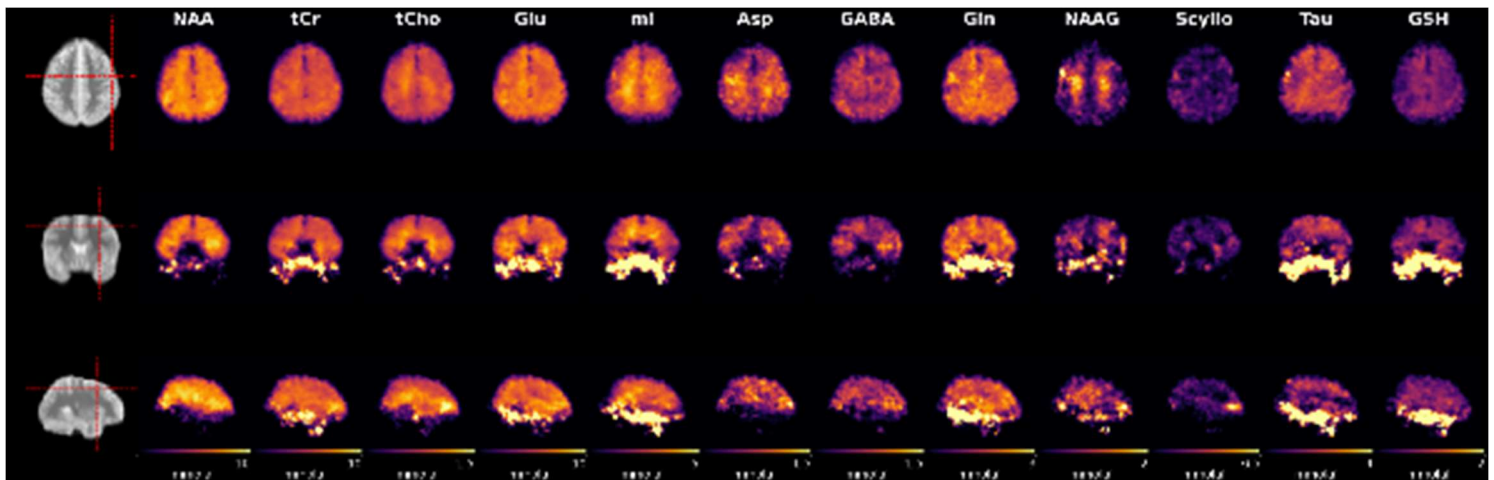
Figure 6: Transversal, coronal, and sagittal median metabolite maps [mmol kg⁻¹]. Red dashed lines on the anatomical figures show the slices selected for display. All maps have 0 as the minimum and displayed with the max value for the maps noted on the color bars.

(Figure 4), there appears to be an increased concentration of NAA in WM compared to grey matter. These differences observed in the metabolite maps are substantiated with the statistical testing highlighting increased NAA in the parietal lobe WM compared to the GM of the frontal, parietal, and occipital lobes.

By considering Figure 2, it is possible to ascertain further insights into metabolite distributions. Metabolites with CRLBs that appear with a strong tissue contrast provide a hint that regions with an increase in CRLB are less likely to confidently fit a metabolite due to its lower regional concentration. For instance, NAAG is well documented to be almost exclusively located in the WM in MRSI studies (Bogner et al., 2012; Hangel et al., 2021; Henning et al., 2009; Nassirpour et al., 2016; Wright et al., 2022; Ziegs et al., 2023), and this is strongly supported in the present cohort by both the metabolite and CRLB maps. Metabolites with interesting CRLB map contrasts reflecting GM − WM differences can be observed for

NAAG, Gln, Tau, and Scyllo. This information could be beneficial in tailoring fitting basis vectors to include the most relevant metabolite information to improve fitting accuracy.

4.2 Regional Spectra and Metabolite Concentrations

This work builds on the process of reporting quantitative metabolite concentrations from ^{1}H MRSI data by means of voxel-specific T_1-corrections. A detailed description of these corrections is reported by (Wright et al., 2022), and has been developed further to format the data so that it can be transformed to standard brain spaces. Previous MRSI studies tend to report results in non-quantitative units, with average T_1-corrections, and with LCModel estimated MMs (Bogner et al., 2012; Gasparovic et al., 2006; Hangel et al., 2021; Henning et al., 2009; Maudsley et al., 2009; Nassirpour et al., 2016).

Regional spectra have good spectral resolution with particularly sharp peaks in WM regions. The broader lineshapes in GM regions are most likely attributable to the voxels on the periphery of the brain which are more susceptible to B0 inhomogeneities. Additionally, GM regions included significantly more voxels dispersed across a larger spatial region, of which many are on the periphery of the brain. The interior WM regions are thus less susceptible to lipid contributions and are comprised of fewer spectra due to the more compact volume of the available atlases. An atlas partitioned into WM regions for use with spectroscopy data sets would allow for the inclusion of more voxels in WM regional spectra.

Future efforts could control spectral quality in an autonomous fashion by considering the linewidths of key peaks, or by considering a spectrum's match to a control spectrum using a prediction model. However, this likely would not be necessary, and regional spectra quality (specifically SNR) could be expected to improve by collecting more data and improving B_0 shimming.

Magnetic resonance spectroscopy studies generally report metabolite concentrations in absolute concentrations in either molal (often, mmol kg^{-1}) or molar (often, mM) quantities (Near et al., 2020). Regional concentrations estimated in this work are compared to previous single voxel ^{1}H MRS and ^{1}H MRSI studies in Table 5 [mmol kg^{-1}] and Table 6 [mM]. Metabolite concentrations derived herein are in general agreement with previous studies cited in Table 5 and Table 6.

While metabolite maps show tissue contrast for NAA, tCho, NAAG, Glu, and Gln, metabolite concentrations in Table 2, Figure 4, and Supporting Information Table 2, the differences between GM and WM regions are generally minor if relaxation corrections are considered. NAA, tCho, mI, and Asp are present in higher concentrations in the frontal lobe WM, occipital lobe WM, and parietal lobe WM. In GM regions, it would be expected for Glu and Gln to display and be presented in higher concentrations compared to the concentrations in WM regions. While this is not as obvious for all regions in Table 2, violin plots and metabolite maps (Figure 1) display tissue contrast for Glu and somewhat for Gln; where Glu is elevated in the frontal lobe GM and parietal lobe GM compared to the parietal lobe WM (Table 2 and Figure 4). However, more data and controls for Glu and Gln fitting quality are needed to decisively quantify the concentration differences for Glu and Gln between GM and WM regions.

mI is reduced in GM compared to previous works (Deelchand et al., 2010; Hangel et al., 2021; Kreis et al., 1993; Le Lecocq et al., n.d.; Mekle et al., 2009; Murali-Manohar et al., 2020); this arises from the difference of how these studies accounted for macromolecules. In this work, the MM$_{AXIOM}$ has macromolecule resonances included between 3.4 and 4.0 ppm that result in a reduction of the fitting

area for mI, while prior works neglected to include macromolecule resonances which affect the resonances between 3.4 and 4.0 ppm. A similar effect can be seen for NAA, albeit this is not as strong of an effect. Of the available comparisons in Table 5, the metabolite concentrations here tend to be lower. The concentrations are generally overlapping when considering the standard deviations in conjunction with the means between studies. The study from (Minati et al., 2010) reported much higher concentrations than other works. It is also important to note that the herein presented work considers tissue-specific T_1-corrections for each voxel (Wright et al., 2022), which showed a contrast shift for Glu and mI which are reported to have a strong T_1-relaxation time tissue dependence (Wright, Murali-Manohar, et al., 2021). Within this work, statistical tests affirm that mI concentrations are increased in the occipital lobe WM compared to frontal lobe GM, occipital lobe GM, and parietal lobe GM; additionally, the parietal lobe WM concentrations are higher than the occipital lobe GM concentrations.

The herein obtained results generally agree with previous studies both at UHF and otherwise. Inter-subject CVs in Table 4 show that it is possible to confidently (CV < 10%) measure NAA, tCr, Glu, mI, tCho, Gln, GABA and Tau in a variety of major brain regions. While NAAG has a CV greater than 10% in all regions, metabolite maps have routinely showed NAAG spatially located in the WM (Bogner et al., 2012; Hangel et al., 2021; Henning et al., 2009; Nassirpour et al., 2016; Wright et al., 2022; Ziegs et al., 2023); acquiring more data could help to increase the confidence in NAAG concentration estimations.

More specifically, metabolite concentrations estimated in this study are in rough agreement with those previously acquired with the same methodology at 9.4 T (Wright et al., 2022). A noticeable shift is present, with many of the concentrations being slightly higher in this work. One notable characteristic in the concentration distributions (Figure 5) is an uneven density of concentrations biased towards lower values for metabolites with low peak intensities including GABA, NAAG, Scyllo or Asp. Recent and, so far, unpublished investigations have shown that this bias is caused by the LCmodel spectral fitting algorithm.

Metabolite concentration comparisons [mmol kg⁻¹]											
	NAA	tCr	Glu	mI	tCho	Gln	NAAG	Asp	GABA	GSH	Tau	Scyllo
Frontal Lobe GM												
this work	9.39 ± 0.73	7.57 ± 0.32	8.41 ± 0.39	4.06 ± 0.49	1.08 ± 0.08	2.37 ± 0.26	1.78 ± 0.92	1.02 ± 0.18	0.86 ± 0.08	0.96 ± 0.12	2.64 ± 0.51	0.3 ± 0.04
Frontal Lobe WM												
this work	11.16 ± 0.34	9.54 ± 0.66	9.5 ± 0.76	5.24 ± 0.96	1.66 ± 0.11	3.22 ± 0.57	3.09 ± 1.49	1.63 ± 0.31	1.38 ± 0.16	1.63 ± 0.34	5.94 ± 7.16	0.44 ± 0.05
Motor cortex (WM-rich)												
Marjanska 2012	10.5 ± 1.2	7.4 ± 0.6	7.6 ± 0.9	5.9 ± 0.3	1.3 ± 0.1	1.0 ± 0.3	1.6 ± 0.4	2.6 ± 0.3	0.8 ± 0.6	0.7 ± 0.1		0.21 ± 0.1
Parietal Lobe GM												
this work	10.23 ± 0.69	8.48 ± 0.37	9.07 ± 0.41	4.14 ± 0.41	1.14 ± 0.08	2.63 ± 0.33	1.65 ± 0.54	1.12 ± 0.27	1.0 ± 0.1	1.03 ± 0.16	2.76 ± 0.32	0.31 ± 0.03
Michaelis 1993	9.8 ± 1.4	6.6 ± 1.0	9.3 ± 2.1	4.7 ± 0.8	1.1 ± 0.3		0.0 ± 0.0					0.4 ± 0.1
Parietal Lobe WM												
this work	12.4 ± 0.62	9.5 ± 0.79	9.34 ± 1.51	5.03 ± 0.77	1.6 ± 0.12	3.22 ± 0.97	2.92 ± 1.05	1.71 ± 0.35	1.44 ± 0.27	1.28 ± 0.2	4.25 ± 2.01	0.49 ± 0.09
Michaelis 1993	7.8 ± 0.7	5.3 ± 0.7	6.6 ± 1.2	3.9 ± 0.9	1.6 ± 0.3		2.2 ± 0.8					0.3 ± 0.1
Occipital Lobe GM												
this work	10.4 ± 1.2	8.02 ± 0.74	8.94 ± 1.48	3.62 ± 0.46	1.0 ± 0.14	2.74 ± 1.08	2.07 ± 0.79	0.8 ± 0.4	0.83 ± 0.21	1.08 ± 0.33	2.78 ± 0.91	0.37 ± 0.1
Deelchand 2010	13.5 ± 1.6	7.7 ± 0.4	9.3 ± 0.9	5.3 ± 0.4	0.9 ± 0.2	2.2 ± 0.2	1.1 ± 0.5	2.1 ± 0.5	1.3 ± 0.4	1.1 ± 0.3	1.3 ± 0.2	0.3 ± 0.2
Mekle 2009	11.8 ± 0.2	8.0 ± 0.4	9.9 ± 0.9	5.7 ± 0.5	1.1 ± 0.5	2.2 ± 0.4	1.1 ± 0.4	2.9 ± 0.5	1.3 ± 0.2	1.3 ± 0.2	1.5 ± 0.3	0.3 ± 0.1
Murali-Manohar 2020	12.6 ± 1.0	10.1 ± 0.5	10.9 ± 0.8	5.2 ± 0.5	1.0 ± 0.1		1.4 ± 0.2	4.8 ± 1.2	1.9 ± 0.9	1.7 ± 0.2	1.6 ± 0.4	0.1 ± 0.1
Wright 2021	12.5 ± 0.7	10.0 ± 1.1	13.0 ± 1.5	4.2 ± 0.8	1.2 ± 0.2		1.8 ± 0.5	5.8 ± 0.6	1.9 ± 0.5	1.4 ± 0.3	1.5 ± 0.5	0.1 ± 0.05
Occipital Lobe WM												
this work	11.27 ± 0.69	8.91 ± 0.68	8.05 ± 0.4	5.63 ± 0.99	1.57 ± 0.16	3.06 ± 0.72	2.47 ± 0.6	1.33 ± 0.38	1.11 ± 0.27	1.3 ± 0.2	3.41 ± 1.38	0.29 ± 0.07
Wright 2021	11.8 ± 1.1	9.2 ± 0.8	10.9 ± 1.1	5.0 ± 0.6	1.8 ± 0.2		2.6 ± 0.4	4.8 ± 0.7	1.2 ± 0.7	1.5 ± 0.3	1.0 ± 0.4	0.1 ± 0.1
Occipital Lobe												
Mangia 2006	10.8 ± 0.1	8.4 ± 0.3	11.0 ± 0.1	6.7 ± 0.1	1.3 ± 0.0	2.9 ± 0.1	1.4 ± 0.0	1.0 ± 0.2	1.0 ± 0.0	1.0 ± 0.1	1.9 ± 0.1	0.4 ± 0.0
Terpstra 2009	12.4 ± 0.7	8.4 ± 0.3	8.9 ± 0.3		1.0 ± 0.3	2.5 ± 0.2	1.2 ± 0.2	2.0 ± 0.4	0.9 ± 0.1	0.7 ± 0.1	1.7 ± 0.2	0.3 ± 0.1
Marjanksa 2012	12.6 ± 1.7	8.7 ± 1.1	9.6 ± 1.3	6.4 ± 0.8	0.9 ± 0.1	1.5 ± 0.5	0.4 ± 0.2	2.9 ± 0.8	1.5 ± 0.3	1.1 ± 0.1		0.4 ± 0.1

Corpus Callosum												
this work	8.64 ± 1.47	7.15 ± 1.08	7.24 ± 1.27	4.36 ± 0.71	1.18 ± 0.22	2.29 ± 0.59	2.26 ± 0.96	0.92 ± 0.35	0.83 ± 0.2	1.0 ± 0.23	7.5 ± 14.68	0.28 ± 0.06
Temporal Lobe GM												
this work	9.99 ± 0.66	10.76 ± 6.33	14.15 ± 12.98	8.65 ± 8.89	1.22 ± 0.12	8.01 ± 13.19	2.8 ± 1.3	0.82 ± 0.26	0.85 ± 0.16	3.51 ± 3.84	22.16 ± 26.51	0.36 ± 0.04
Average GM												
This work	9.8 ± 0.69	8.01 ± 0.22	8.64 ± 0.43	4.03 ± 0.47	1.1 ± 0.07	2.47 ± 0.3	1.82 ± 0.73	1.03 ± 0.17	0.9 ± 0.07	1.0 ± 0.13	2.71 ± 0.57	0.32 ± 0.03
Average WM												
This work	10.7 ± 0.66	8.75 ± 0.56	8.43 ± 0.82	4.97 ± 0.67	1.5 ± 0.13	2.82 ± 0.59	2.5 ± 0.82	1.24 ± 0.31	1.09 ± 0.12	1.25 ± 0.19	2.76 ± 0.4	0.36 ± 0.04

Table 5: Metabolite concentration comparisons from studies reporting results in [mmol kg^{-1}]. Citations: (Deelchand et al., 2010; Mangia et al., 2006; Marjańska et al., 2012; Mekle et al., 2009; Michaelis et al., 1993; Murali-Manohar et al., 2020; Terpstra et al., 2009; Wright et al., 2022; Wright, Murali-Manohar, et al., 2021)

Metabolite concentration comparisons [mM]

	NAA	tCr	Glu	mI	tCho	Gln	NAAG	Asp	GABA	GSH	Tau	Scyllo
Frontal Lobe GM												
this work	6.99 ± 0.47	5.68 ± 0.22	6.3 ± 0.26	3.06 ± 0.36	0.8 ± 0.06	1.73 ± 0.2	1.34 ± 0.67	0.75 ± 0.12	0.63 ± 0.06	0.7 ± 0.09	1.96 ± 0.37	0.24 ± 0.03
Hangel 2021	9.44 ± 3.98	6.98 ± 3.01	8.29 ± 3.98	5.33 ± 2.29	1.74 ± 0.79							
Lecocq 2015	10.03 ± 1.71	7.29 ±1.69		5.30 ± 2.67	1.78 ± 0.55							
Frontal Lobe WM												
this work	7.6 ± 0.28	6.48 ± 0.42	6.47 ± 0.52	3.55 ± 0.63	1.12 ± 0.08	2.19 ± 0.38	2.06 ± 0.99	1.11 ± 0.23	0.93 ± 0.1	1.1 ± 0.22	4.07 ± 4.69	0.31 ± 0.04
Hangel 2021	9.91 ± 3.81	7.39 ± 2.69	7.99 ± 3.41	5.20 ± 1.92	1.99 ± 0.79							
Minati 2010	14.20 ± 2.00	11.50 ± 2.40		7.60 ± 2.00	3.60 ± 0.80							
Parietal Lobe GM												
this work	7.59 ± 0.44	6.26 ± 0.28	6.71 ± 0.3	3.07 ± 0.3	0.84 ± 0.06	1.91 ± 0.23	1.21 ± 0.41	0.82 ± 0.2	0.73 ± 0.07	0.75 ± 0.11	2.04 ± 0.2	0.24 ± 0.02
Hangel 2021	10.09 ± 3.02	7.57 ± 2.23	8.55 ± 2.81	5.61 ± 1.63	1.64 ± 0.50							
Parietal Lobe WM												
this work	8.26 ± 0.41	6.33 ± 0.54	6.25 ± 1.04	3.34 ± 0.5	1.06 ± 0.08	2.15 ± 0.65	1.93 ± 0.71	1.14 ± 0.24	0.96 ± 0.18	0.85 ± 0.14	2.86 ± 1.44	0.33 ± 0.06
Hangel 2021	10.21 ± 2.66	7.51 ± 2.00	7.64 ± 2.61	5.54 ± 1.38	1.84 ± 0.51							
Minati 2010	14.00 ± 1.80	10.70 ± 1.50		5.80 ± 2.00	2.90 ± 0.40							
Parietal Lobe												
Hangel 2021	10.15 ± 2.83	7.54 ± 2.11	8.07 ± 2.74	5.58 ± 1.50	1.74 ± 0.52							
Volk 2018	11.59 ± 0.13	7.54 ± 0.14	12.55 ± 0.22	3.70 ± 0.08	1.65 ± 0.05							
Occipital Lobe GM												
this work	7.83 ± 0.67	6.04 ± 0.47	6.81 ± 1.31	2.79 ± 0.4	0.74 ± 0.1	2.0 ± 0.85	1.56 ± 0.54	0.59 ± 0.29	0.61 ± 0.15	0.8 ± 0.29	1.88 ± 0.51	0.29 ± 0.08
Hangel 2021	8.58 ± 4.31	6.55 ± 2.92	7.26 ± 3.72	4.57 ± 2.00	1.46 ± 0.65							

Pouwels 1998	9.20 ± 0.90	6.90 ± 0.70	8.60 ± 1.10	4.10 ± 0.60	0.88 ± 0.10							
Kreis 1993	9.06 ± 0.12	7.95 ± 0.11		6.24 ± 0.21	1.41 ± 0.05							
Occipital Lobe WM												
this work	7.53 ± 0.44	5.91 ± 0.45	5.4 ± 0.28	3.74 ± 0.64	1.04 ± 0.11	2.02 ± 0.47	1.62 ± 0.4	0.88 ± 0.25	0.74 ± 0.18	0.86 ± 0.13	2.33 ± 1.06	0.22 ± 0.04
Hangel 2021	8.83 ± 3.91	6.61 ± 2.66	6.68 ± 3.35	4.59 ± 1.79	1.61 ± 0.68							
Pouwels 1998	7.80 ± 0.90	5.50 ± 0.80	6.00 ± 1.20	4.10 ± 0.80	1.64 ± 0.21							
Corpus Callosum												
this work	6.16 ± 0.77	5.02 ± 0.65	5.09 ± 0.83	3.04 ± 0.44	0.8 ± 0.15	1.54 ± 0.4	1.53 ± 0.64	0.62 ± 0.23	0.56 ± 0.13	0.67 ± 0.16	5.09 ± 9.9	0.21 ± 0.04
Hangel 2021	9.50 ± 4.28	5.93 ± 2.62	6.54 ± 3.46	5.35 ± 2.31	2.07 ± 0.88							
Temporal Lobe GM												
this work	7.39 ± 0.44	8.06 ± 4.65	10.67 ± 9.88	6.32 ± 6.21	0.91 ± 0.09	5.76 ± 9.41	2.08 ± 0.94	0.62 ± 0.19	0.63 ± 0.12	2.47 ± 2.56	15.89 ± 18.66	0.28 ± 0.03
Hangel 2021	8.33 ± 4.63	6.74 ± 3.19	7.47 ± 3.91	4.82 ± 2.21	1.84 ± 0.87							
Lecocq 2015	9.84 ± 0.77	8.01 ± 0.43		4.75 ± 0.40	1.94 ± 0.36							
Average GM												
This work	7.28 ± 0.45	5.98 ± 0.16	6.46 ± 0.3	3.03 ± 0.35	0.82 ± 0.05	1.79 ± 0.21	1.35 ± 0.54	0.76 ± 0.13	0.66 ± 0.05	0.73 ± 0.09	2.0 ± 0.4	0.25 ± 0.02
Average WM												
This work	7.32 ± 0.37	5.92 ± 0.37	5.77 ± 0.56	3.36 ± 0.44	1.01 ± 0.09	1.9 ± 0.39	1.67 ± 0.54	0.84 ± 0.21	0.74 ± 0.09	0.84 ± 0.13	1.9 ± 0.28	0.27 ± 0.03

Table 6: Metabolite concentration comparisons from studies reporting results in [mM]. Citations: (Hangel et al., 2021; Kreis et al., 1993; Le Lecocq et al., n.d.; Minati et al., 2010; Pouwels & Frahm, 1998; Volk et al., 2018)

4.3 Limitations

This study aimed to achieve whole-brain coverage including cerebrum and cerebellum for metabolite mapping using a ^{1}H FID-MRSI sequence; however, data quality was insufficient in lower slices to report reliable results. Thus, only cerebrum coverage was considered and yielded metabolite maps and regional concentrations for 12 metabolites. In general, data below slice 48 of the MNI space images which corresponds to below MRSI slice 10 were more prone to distortions that degraded metabolite image quality. A potential solution for this problem would be using an RF coil with improved longitudinal coverage and metabolite SNR in lower slices and most importantly improved B_0 shimming (Motyka et al., 2019).
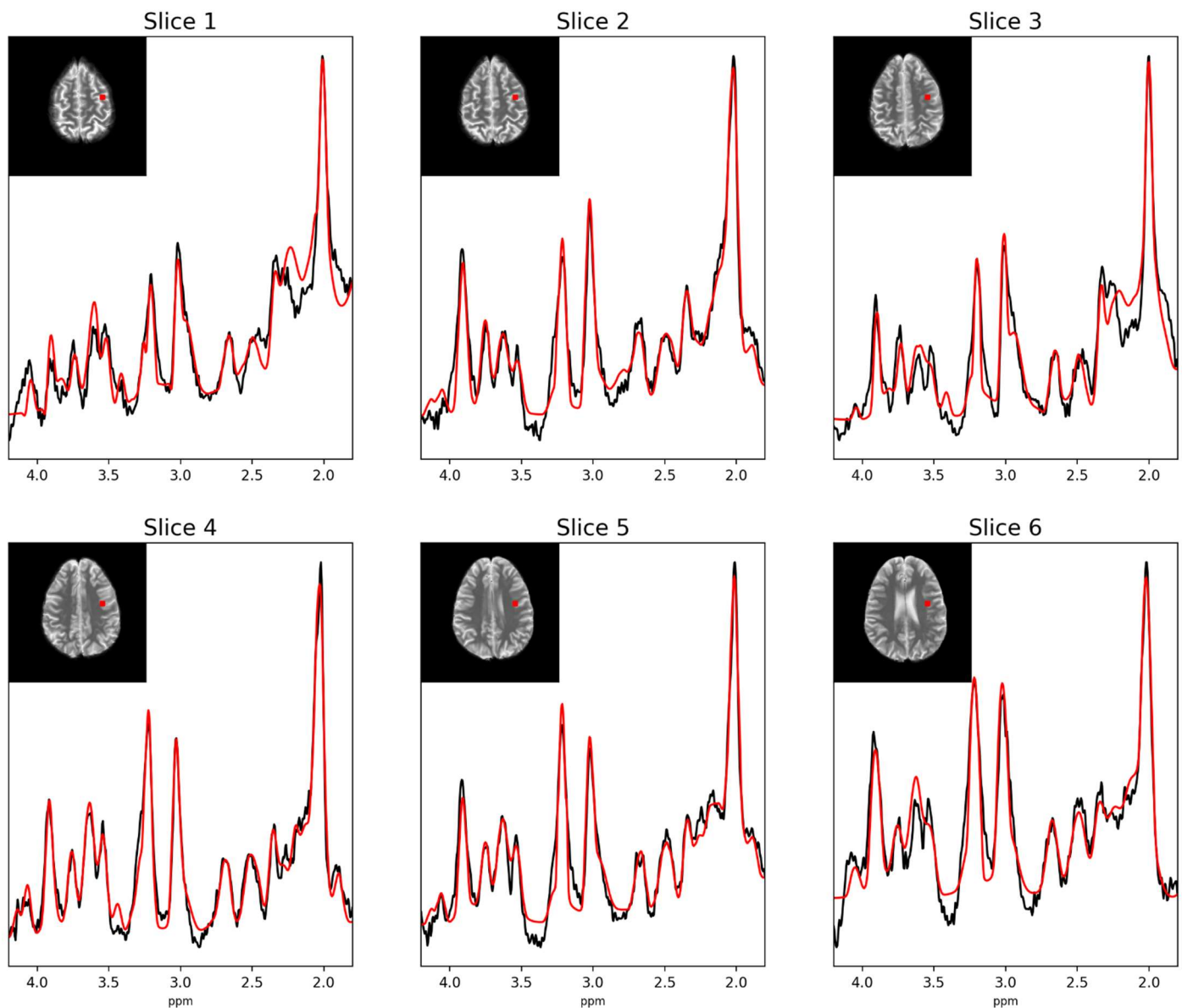
Figure 7: individual fitted voxels in the same matrix position (coronal: 15, sagittal: 24) across slices 1 to 6 from one volunteer. The red square shows the voxel position with roughly the same dimensions as the in vivo voxel.
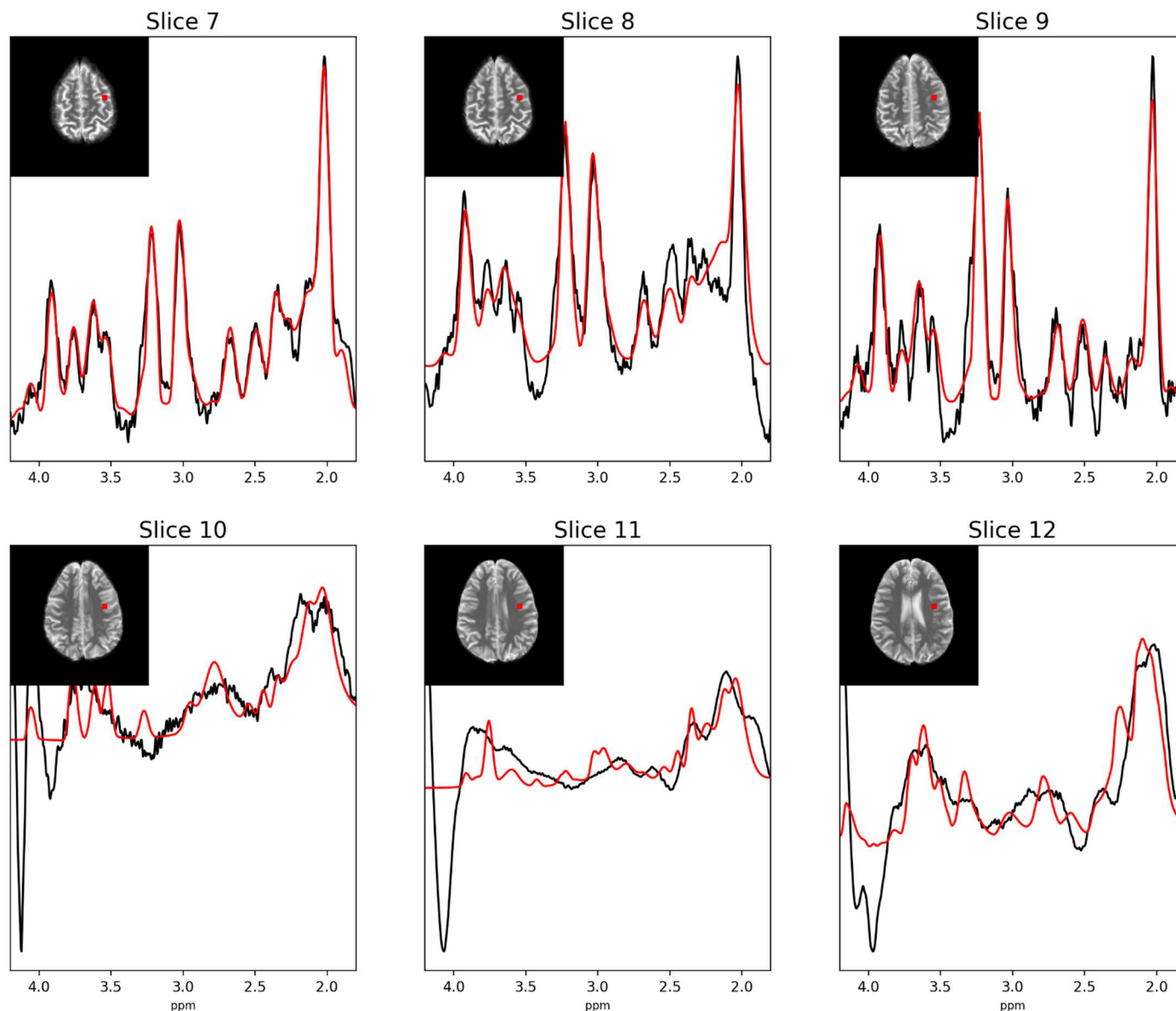
Figure 8: individual fitted voxels in the same matrix position (coronal: 15, sagittal: 24) across slices 7 to 12 from the same volunteer as in Figure 7. The red square shows the voxel position with roughly the same dimensions as the in vivo voxel. Note the dramatic shift in acquisition quality below slice 9 for this volunteer (not included in analysis).

For illustrative purposes, Figure 7 and Figure 8 show the same coronal (15) and sagittal (25) voxel position across 12 transversal positions corresponding to respective MRSI slices acquired in one volunteer. As can be seen spectra in slices $1 - 9$ (top to bottom) is good, the spectral line width starts to get very wide in slice 10 and after slice 10 the metabolite information is lost. For most volunteers, the data quality dropped similarly between slice 9 and slice 11. Improvements in B_0 shimming and increased SNR in the lower slices of the brain could help to improve measurement quality and provide an avenue to investigate lower brain regions when part of full brain studies (Motyka et al., 2019).

In general, techniques such as motion correction (Moser et al., 2020) could dramatically reduce the CV for metabolite concentration estimates. Another strategy using MRSI could be to extract and sum region

specific voxels in the step directly prior to fitting spectra (Schreiner et al., 2016, 2018). This could improve metabolite fitting performance in LCModel and therefore reduce inter-subject CVs.

From an analysis perspective, the WM atlas used to estimate WM concentrations is a tractography atlas, and the WM volumes do not include all WM tissue within brain regions. Developing a more appropriate atlas for MRSI studies could increase the number of WM voxels included in concentration estimates.

Finally, the inclusion of a larger number of volunteers in a future study could further increase the accuracy and precision of region specific metabolite concentration estimates in the entire brain.

5   Conclusion and outlook

The methods used in this study are a culmination of previous works that developed short TR, ^{1}H FID MRSI at 9.4 T and reports group averaged quantitative ^{1}H MRSI acquired in the human brain at 9.4 T with full cerebrum coverage for the first time. Co-registering MRSI data to the MNI space can positively contribute to further characterization of the concentrations and standardized reporting of the distributions of metabolites in the human brain. By reporting results in a standard space and applying full relaxation correction to the metabolite maps, future works would be able to characterize and compare regional spectra as well as combine metabolite maps across studies. Pooling ^{1}H MRSI data from healthy volunteer and patient cohorts via this approach could bring more power to studies investigating differences between healthy and diseased populations in future and would also serve as a means to directly compare MRSI acquisition and quantification techniques.

References:

Avdievich, N. I., Giapitzakis, I.-A., Pfrommer, A., & Henning, A. (2018). Decoupling of a tight-fit transceiver phased array for human brain imaging at 9.4T: Loop overlapping rediscovered. *Magnetic Resonance in Medicine*, *79*(2), 1200–1211. https://doi.org/10.1002/mrm.26754

Bilgic, B., Chatnuntawech, I., Fan, A. P., Setsompop, K., Cauley, S. F., Wald, L. L., & Adalsteinsson, E. (2014). Fast image reconstruction with L2-regularization. *Journal of Magnetic Resonance Imaging*, *40*(1), 181–191. https://doi.org/10.1002/jmri.24365

Bogner, W., Gruber, S., Trattnig, S., & Chmelik, M. (2012). *High-resolution mapping of human brain metabolites by free induction decay 1 H MRSI at 7 T*. May 2011, 873–882. https://doi.org/10.1002/nbm.1805

Bogner, W., Otazo, R., & Henning, | Anke. (2020). *Accelerated MR spectroscopic imaging-a review of current and emerging techniques*. https://doi.org/10.1002/nbm.4314

Bydder, M., Hamilton, G., Yokoo, T., & Sirlin, C. B. (2008). Optimal phased-array combination for spectroscopy. *Magnetic Resonance Imaging*, *26*(6), 847–850. https://doi.org/10.1016/j.mri.2008.01.050

Cabanes, E., Confort-Gouny, S., Le Fur, Y., Simond, G., & Cozzone, P. J. (2001). Optimization of residual water signal removal by HLSVD on simulated short echo time proton MR spectra of the human brain. *Journal of Magnetic Resonance*, *150*(2), 116–125. https://doi.org/10.1006/jmre.2001.2318

Deelchand, D. K., Moortele, P. F. Van De, Adriany, G., Iltis, I., Andersen, P., Henry, P. G., Strupp, J. P., Vaughan, J. T., Ug, K., Thomas Vaughan, J., Uurbil, K., & Henry, P. G. (2010). In vivo1H NMR spectroscopy of the human brain at 9.4 T: Initial results. *Journal of Magnetic Resonance*, *206*(1), 74–80. https://doi.org/10.1016/j.jmr.2010.06.006

Desikan, R. S., Cabral, H. J., Settecase, F., Hess, C. P., Dillon, W. P., Glastonbury, C. M., Weiner, M. W., Schmansky, N. J., Salat, D. H., & Fischl, B. (2010). Automated MRI measures predict progression to Alzheimer's disease. *Neurobiology of Aging*, *31*(8), 1364. https://doi.org/10.1016/J.NEUROBIOLAGING.2010.04.023

Frazier, J. A., Chiu, S., Breeze, J. L., Makris, N., Lange, N., Kennedy, D. N., Herbert, M. R., Bent, E. K., Koneru, V. K., Dieterich, M. E., Hodge, S. M., Rauch, S. L., Grant, P. E., Cohen, B. M., Seidman, L. J., Caviness, V. S., & Biederman, J. (2005). Structural brain magnetic resonance imaging of limbic and thalamic volumes in pediatric bipolar disorder. *The American Journal of Psychiatry*, *162*(7), 1256–1265. https://doi.org/10.1176/APPI.AJP.162.7.1256

Gasparovic, C., Song, T., Devier, D., Bockholt, H. J., Caprihan, A., Mullins, P. G., Posse, S., Jung, R. E., & Morrison, L. A. (2006). Use of tissue water as a concentration reference for proton spectroscopic imaging. *Magnetic Resonance in Medicine*, *55*(6), 1219–1226. https://doi.org/10.1002/mrm.20901

Goldstein, J. M., Seidman, L. J., Makris, N., Ahern, T., O'Brien, L. M., Caviness, V. S., Kennedy, D. N., Faraone, S. V., & Tsuang, M. T. (2007). Hypothalamic abnormalities in schizophrenia: sex effects and genetic vulnerability. *Biological Psychiatry*, *61*(8), 935–945. https://doi.org/10.1016/J.BIOPSYCH.2006.06.027

Gruber, S., Heckova, E., Strasser, B., Považan, M., Hangel, G. J., Minarikova, L., Trattnig, S., & Bogner, W. (2017). Mapping an Extended Neurochemical Profile at 3 and 7 T Using Accelerated High-Resolution Proton Magnetic Resonance Spectroscopic Imaging. *Investigative Radiology*, *52*(10), 631–639. https://doi.org/10.1097/RLI.0000000000000379

Hagberg, G. E., Bause, J., Ethofer, T., Ehses, P., Dresler, T., Herbert, C., Pohmann, R., Shajan, G., Fallgatter, A., Pavlova, M. A., & Scheffler, K. (2017). Whole brain MP2RAGE-based mapping of the longitudinal relaxation time at 9.4T. *NeuroImage*, *144*, 203–216. https://doi.org/10.1016/j.neuroimage.2016.09.047

Hangel, G., Cadrien, C., Lazen, P., Furtner, J., Lipka, A., Hečková, E., Hingerl, L., Motyka, S., Gruber, S., Strasser, B., Kiesel, B., Mischkulnig, M., Preusser, M., Roetzer, T., Wöhrer, A., Widhalm, G., Rössler, K., Trattnig, S., & Bogner, W. (2020). High-resolution metabolic imaging of high-grade gliomas using 7T-CRT-FID-MRSI. *NeuroImage: Clinical*, *28*, 102433. https://doi.org/10.1016/J.NICL.2020.102433

Hangel, G., Spurny-Dworak, B., Lazen, P., Cadrien, | Cornelius, Sharma, S., Lukas Hingerl, |, Hečková, | Eva, Strasser, | Bernhard, Stanislav Motyka, |, Lipka, A., Gruber, S., Brandner, C., Lanzenberger, | Rupert, Rössler, K., Trattnig, | Siegfried, & Bogner, W. (2021). *Inter-subject stability and regional concentration estimates of 3D-FID-MRSI in the human brain at 7 T*. https://doi.org/10.1002/nbm.4596

Heckova, E., Dal-Bianco, A., Strasser, B., Hangel, G. J., Lipka, A., Motyka, S., Hingerl, L., Rommer, P. S., Berger, T., Hnilicová, P., Kantorová, E., Leutmezer, F., Kurča, E., Gruber, S., Trattnig, S., & Bogner, W. (2022). Extensive Brain Pathologic Alterations Detected with 7.0-T MR Spectroscopic Imaging Associated with Disability in Multiple Sclerosis. *Radiology*, *303*(1), 141–150. https://doi.org/10.1148/RADIOL.210614/ASSET/IMAGES/LARGE/RADIOL.210614FIG6.JPEG

Henning, A. (2017). Proton and multinuclear magnetic resonance spectroscopy in the human brain at ultra-high field strength: A review. *NeuroImage*, *168*, 181–198. https://doi.org/10.1016/j.neuroimage.2017.07.017

Henning, A., Fuchs, A., Murdoch, J. B., & Boesiger, P. (2009). Slice-selective FID acquisition, localized by outer volume suppression (FIDLOVS) for 1H-MRSI of the human brain at 7 T with minimal signal loss. *NMR in Biomedicine*, *22*(7), 683–696. https://doi.org/10.1002/nbm.1366

Hua, K., Zhang, J., Wakana, S., Jiang, H., Li, X., Reich, D. S., Calabresi, P. A., Pekar, J. J., van Zijl, P. C. M., & Mori, S. (2008). Tract probability maps in stereotaxic spaces: analyses of white matter anatomy and tract-specific quantification. *NeuroImage*, *39*(1), 336–347. https://doi.org/10.1016/J.NEUROIMAGE.2007.07.053

Jenkinson, M., Beckmann, C. F., Behrens, T. E. J., Woolrich, M. W., & Smith, S. M. (2012). FSL. *NeuroImage*, *62*(2), 782–790. https://doi.org/10.1016/J.NEUROIMAGE.2011.09.015

Kay, S. M. (1988). *Modern spectral estimation: theory and application*. Pearson Education India.

Klauser, A., Strasser, B., Thapa, B., Lazeyras, F., & Andronesi, O. (2021). Achieving high-resolution 1H-MRSI of the human brain with compressed-sensing and low-rank reconstruction at 7 Tesla. *Journal of Magnetic Resonance (San Diego, Calif. : 1997)*, *331*, 107048. https://doi.org/10.1016/J.JMR.2021.107048

Klose, U. (1990). In vivo proton spectroscopy in presence of eddy currents. *Magnetic Resonance in Medicine*, *14*(1), 26–30. https://doi.org/10.1002/mrm.1910140104

Kreis, R., Ernst, T., & Ross, B. D. (1993). Absolute Quantitation of Water and Metabolites in the Human Brain. II. Metabolite Concentrations. In *Journal of Magnetic Resonance, Series B* (Vol. 102, Issue 1, pp. 9–19). https://doi.org/10.1006/jmrb.1993.1056

Laino, M. E., Young, R., Beal, K., Haque, S., Mazaheri, Y., Corrias, G., Bitencourt, A. G., Karimi, S., & Thakur, S. B. (2020). Magnetic resonance spectroscopic imaging in gliomas: clinical diagnosis and radiotherapy planning. *Https://Doi.Org/10.1259/Bjro.20190026*, *2*(1), 20190026. https://doi.org/10.1259/BJRO.20190026

Le Lecocq, A., Le Fur, Y., Maudsley, A. A., Le Troter, A., Sheriff, S., Sabati, M., Donnadieu, M., Confort-Gouny, S., Cozzone, P. J., Guye, M., & Ranjeva, J.-P. (n.d.). *Whole-Brain Quantitative Mapping of Metabolites Using Short Echo Three-Dimensional Proton MRSI*. https://doi.org/10.1002/jmri.24809

Lin, A., Andronesi, O., Bogner, W., Choi, I. Y., Coello, E., Cudalbu, C., Juchem, C., Kemp, G. J., Kreis, R., Krššák, M., Lee, P., Maudsley, A. A., Meyerspeer, M., Mlynarik, V., Near, J., Öz, G., Peek, A. L., Puts, N. A., Ratai, E. M., … Mullins, P. G. (2021). Minimum Reporting Standards for in vivo Magnetic Resonance Spectroscopy (MRSinMRS): Experts' consensus recommendations. *NMR in Biomedicine*, *34*(5). https://doi.org/10.1002/NBM.4484

Makris, N., Goldstein, J. M., Kennedy, D., Hodge, S. M., Caviness, V. S., Faraone, S. V., Tsuang, M. T., & Seidman, L. J. (2006). Decreased volume of left and total anterior insular lobule in schizophrenia. *Schizophrenia Research*, *83*(2–3), 155–171. https://doi.org/10.1016/J.SCHRES.2005.11.020

Mangia, S., Tkáč, I., Gruetter, R., Van De Moortele, P.-F., Giove, F., Maraviglia, B., & Uğurbil, K. (2006). Sensitivity of single-voxel 1H-MRS in investigating the metabolism of the activated human visual cortex at 7 T. *Magnetic Resonance Imaging*, *24*(4), 343–348. https://doi.org/10.1016/J.MRI.2005.12.023

Marjańska, M., Auerbach, E. J., Valabrègue, R., Van de Moortele, P.-F., Adriany, G., & Garwood, M. (2012). Localized 1H NMR spectroscopy in different regions of human brain in vivo at 7 T: T2 relaxation times and concentrations of cerebral metabolites. *NMR in Biomedicine*, *25*(2), 332–339. https://doi.org/10.1002/nbm.1754

Maudsley, A. A., Andronesi, O. C., Barker, P. B., Bizzi, A., Bogner, W., Henning, A., Nelson, S. J., Posse, S., Shungu, D. C., & Soher, B. J. (2020). *Advanced magnetic resonance spectroscopic neuroimaging: Experts' consensus recommendations*. https://doi.org/10.1002/nbm.4309

Maudsley, A. A., Domenig, C., Govind, V., Darkazanli, A., Studholme, C., Arheart, K., & Bloomer, C. (2009). Mapping of brain metabolite distributions by volumetric proton MR spectroscopic imaging (MRSI). *Magnetic Resonance in Medicine*, *61*(3), 548–559. https://doi.org/10.1002/mrm.21875

Mekle, R., Mlynárik, V., Gambarota, G., Hergt, M., Krueger, G., & Gruetter, R. (2009). MR spectroscopy of the human brain with enhanced signal intensity at ultrashort echo times on a clinical platform at 3T and 7T. *Magnetic Resonance in Medicine*, *61*(6), 1279–1285. https://doi.org/10.1002/mrm.21961

Michaelis, T., Merboldt, K. D., Bruhn, H., Hänicke, W., & Frahm, J. (1993). Absolute concentrations of metabolites in the adult human brain in vivo: quantification of localized proton MR spectra. *Radiology*, *187*(1), 219–227.

Minati, L., Aquino, D., Bruzzone, M. G., & Erbetta, A. (2010). Quantitation of normal metabolite concentrations in six brain regions by in-vivoH-MR spectroscopy. *Journal of Medical Physics*, *35*(3), 154–163. https://doi.org/10.4103/0971-6203.62128

Moser, P., Eckstein, K., Hingerl, L., Weber, M., Motyka, S., Strasser, B., van der Kouwe, A., Robinson, S., Trattnig, S., & Bogner, W. (2020). Intra-session and inter-subject variability of 3D-FID-MRSI using single-echo volumetric EPI navigators at 3T. *Magnetic Resonance in Medicine*, *83*(6), 1920–1929. https://doi.org/10.1002/MRM.28076

Motyka, S., Moser, P., Hingerl, L., Hangel, G., Heckova, E., Strasser, B., Eckstein, K., Daniel Robinson, S., Poser, B. A., Gruber, S., Trattnig, S., & Bogner, W. (2019). The influence of spatial resolution on the spectral quality and quantification accuracy of whole-brain MRSI at 1.5T, 3T, 7T, and 9.4T. *Magnetic Resonance in Medicine*, *82*(2), 551–565. https://doi.org/10.1002/MRM.27746

MRI Atlas of Human White Matter. (2006). *AJNR: American Journal of Neuroradiology*, *27*(6), 1384. /pmc/articles/PMC8133945/

Murali-Manohar, S., Borbath, T., Wright, A. M. A. M., Soher, B., Mekle, R., & Henning, A. (2020). T2 relaxation times of macromolecules and metabolites in the human brain at 9.4 T. *Magnetic Resonance in Medicine*. https://doi.org/10.1002/mrm.28174

Nassirpour, S., Chang, P., Avdievitch, N., Henning, A., & Sahar Nassirpour, C. (2018). *Compressed Sensing for High-Resolution Non-lipid Suppressed 1 H FID MRSI of the Human Brain at 9.4T*. https://doi.org/10.1002/mrm.27225

Nassirpour, S., Chang, P., & Henning, A. (2016). High and ultra-high resolution metabolite mapping of the human brain using 1H FID MRSI at 9.4T. *NeuroImage*, *December*, 1–11. https://doi.org/10.1016/j.neuroimage.2016.12.065

Nassirpour, S., Chang, P., & Henning, A. (2018). MultiNet PyGRAPPA: Multiple neural networks for reconstructing variable density GRAPPA (a 1H FID MRSI study). *NeuroImage*, *183*(April), 336–345. https://doi.org/10.1016/j.neuroimage.2018.08.032

Near, J., Harris, A. D., Juchem, C., Kreis, R., Marjańska, M., Öz, G., Slotboom, J., Wilson, M., & Gasparovic, C. (2020). Preprocessing, analysis and quantification in single-voxel magnetic resonance spectroscopy: experts' consensus recommendations. *NMR in Biomedicine*. https://doi.org/10.1002/nbm.4257

Öz, G., Alger, J. R., Barker, P. B., Bartha, R., Bizzi, A., Boesch, C., Bolan, P. J., Brindle, K. M., Cudalbu, C., Dinçer, A., Dydak, U., Emir, U. E., Frahm, J., Gilberto González, R., Gruber, S., Gruetter, R., Gupta, R. K., Heerschap, A., Henning, A., … Kauppinen, R. A. (2014). Clinical proton MR spectroscopy in central nervous system disorders. *Radiology*, *270*(3), 658–679. https://doi.org/10.1148/RADIOL.13130531

Pan, J. W., Duckrow, R. B., Gerrard, J., Ong, C., Hirsch, L. J., Resor Jr, S. R., Zhang, Y., Petroff, O., Spencer, S., Hetherington, H. P., & Spencer, D. D. (2013). 7T MR spectroscopic imaging in the localization of surgical epilepsy FULL-LENGTH ORIGINAL RESEARCH. *Epilepsia*, *54*(9), 1668–1678. https://doi.org/10.1111/epi.12322

Pohmann, R., & Scheffler, K. (2013). A theoretical and experimental comparison of different techniques for B1 mapping at very high fields. *NMR in Biomedicine*, *26*(3), 265–275. https://doi.org/10.1002/nbm.2844

Pouwels, P. J. W., & Frahm, J. (1998). Regional metabolite concentrations in human brain as determined by quantitative localized proton MRS. *Magnetic Resonance in Medicine*, *39*(1), 53–60.

Provencher, S. W. (2001). Automatic quantitation of localizedin vivo1H spectra with LCModel. *NMR in Biomedicine*, *14*(4), 260–264. https://doi.org/10.1002/nbm.698

Schreiner, S. J., Kirchner, T., Narkhede, A., Wyss, M., Van Bergen, J. M. G., Steininger, S. C., Gietl, A., Leh, S. E., Treyer, V., Buck, A., Pruessmann, K. P., Nitsch, R. M., Hock, C., Henning, A., Brickman, A. M., & Unschuld, P. G. (2018). Brain amyloid burden and cerebrovascular disease are synergistically associated with neurometabolism in cognitively unimpaired older adults. *Neurobiology of Aging*, *63*, 152–161. https://doi.org/10.1016/J.NEUROBIOLAGING.2017.12.004

Schreiner, S. J., Kirchner, T., Wyss, M., Van Bergen, J. M. G., Quevenco, F. C., Steininger, S. C., Griffith, E. Y., Meier, I., Michels, L., Gietl, A. F., Leh, S. E., Brickman, A. M., Hock, C., Nitsch, R. M., Pruessmann, K. P., Henning, A., & Unschuld, P. G. (2016). Low episodic memory performance in cognitively normal elderly subjects is associated with increased posterior cingulate gray matter N-acetylaspartate: a 1H MRSI study at 7 Tesla. *Neurobiology of Aging*, *48*, 195–203. https://doi.org/10.1016/J.NEUROBIOLAGING.2016.08.022

Terpstra, M., Ugurbil, K., & Tkac, I. (2009). Noninvasive quantification of human brain ascorbate concentration using ^{1} H NMR spectroscopy at 7 T. *NMR in Biomedicine*, *23*(3), n/a-n/a. https://doi.org/10.1002/nbm.1423

Volk, C., Jaramillo, V., Merki, R., O'Gorman Tuura, R., & Huber, R. (2018). Diurnal changes in glutamate + glutamine levels of healthy young adults assessed by proton magnetic resonance spectroscopy. *Human Brain Mapping*, *39*(10), 3984–3992. https://doi.org/10.1002/HBM.24225

Wakana, S., Caprihan, A., Panzenboeck, M. M., Fallon, J. H., Perry, M., Gollub, R. L., Hua, K., Zhang, J., Jiang, H., Dubey, P., Blitz, A., van Zijl, P., & Mori, S. (2007). Reproducibility of quantitative tractography methods applied to cerebral white matter. *NeuroImage*, *36*(3), 630–644. https://doi.org/10.1016/J.NEUROIMAGE.2007.02.049

Wright, A. M., Murali Manohar, S., Ziegs, T., & Henning, A. (2021). Relaxation corrected simulated MM model for improved fitting and quantification of 1H FID MRSI data. *2021 ISMRM & SMRT Annual Meeting & Exhibition (ISMRM 2021)*.

Wright, A. M., Murali-Manohar, S., Borbath, T., Avdievich, N. I., & Henning, A. (2021). Relaxation-corrected macromolecular model enables determination of 1H longitudinal T1-relaxation times and concentrations of human brain metabolites at 9.4T. *Magnetic Resonance in Medicine*, *00*, 1–17. https://doi.org/10.1002/mrm.28958

Wright, A. M., Murali-Manohar, S., & Henning, A. (2022). Quantitative T1-relaxation corrected metabolite mapping of 12 metabolites in the human brain at 9.4 T. *NeuroImage*, *263*. https://doi.org/10.1016/J.NEUROIMAGE.2022.119574

Yarnykh, V. L. (2007). Actual flip-angle imaging in the pulsed steady state: A method for rapid three-dimensional mapping of the transmitted radiofrequency field. *Magnetic Resonance in Medicine*, *57*(1), 192–200. https://doi.org/10.1002/mrm.21120

Ziegs, T., Martin Wright, A., Henning, A., Theresia Ziegs, C., & Wright, A. M. (2023). Test–retest reproducibility of human brain multi-slice 1H FID-MRSI data at 9.4T after optimization of lipid regularization, macromolecular model, and spline baseline stiffness. *Magnetic Resonance in Medicine*, *89*(1), 11–28. https://doi.org/10.1002/MRM.29423